

Metal compositions of carbonaceous chondrites

Elishevah van Kooten, Edith Kubik, Julien Sieberte, Benjamin D. Heredia, Tonny B. Thomsen, Frederic Moynier

▶ **To cite this version:**

Elishevah van Kooten, Edith Kubik, Julien Sieberte, Benjamin D. Heredia, Tonny B. Thomsen, et al.. Metal compositions of carbonaceous chondrites. Geochimica et Cosmochimica Acta, 2022, 321, pp.52-77. 10.1016/j.gca.2022.01.008 . insu-03643037

HAL Id: insu-03643037

https://insu.hal.science/insu-03643037

Submitted on 4 Jun 2022

HAL is a multi-disciplinary open access archive for the deposit and dissemination of scientific research documents, whether they are published or not. The documents may come from teaching and research institutions in France or abroad, or from public or private research centers.

L'archive ouverte pluridisciplinaire **HAL**, est destinée au dépôt et à la diffusion de documents scientifiques de niveau recherche, publiés ou non, émanant des établissements d'enseignement et de recherche français ou étrangers, des laboratoires publics ou privés.



Distributed under a Creative Commons Attribution 4.0 International License

Available online at www.sciencedirect.com

ScienceDirect

Geochimica et Cosmochimica Acta 321 (2022) 52–77

Geochimica et Cosmochimica Acta

www.elsevier.com/locate/gca

Metal compositions of carbonaceous chondrites

Elishevah M.M.E. van Kooten [a,b,*], Edith Kubik [a], Julien Siebert [a], Benjamin D. Heredia [c], Tonny B. Thomsen [c], Frédéric Moynier [a]

[a] Université de Paris, Institut de Physique du Globe de Paris, CNRS UMR 7154, 1 rue Jussieu, 75238 Paris, France
[b] Center for Star and Planet Formation, Globe Institute, University of Copenhagen, Øster Voldgade 5-7, 1350 Copenhagen, Denmark
[c] Geological Survey of Denmark, GEUS, Øster Voldgade 10, 1350 Copenhagen, Denmark

Received 13 January 2021; accepted in revised form 10 January 2022; available online 19 January 2022

Abstract

FeNi metals represent an important fraction of chondritic components that remains relatively unexplored within most carbonaceous chondrite groups. The compositions of these metals can place constraints on the nature of their precursor materials as well as the physicochemical conditions of chondrule formation. In this study, we have analyzed the major, minor and trace element compositions of metal grains from relatively unaltered carbonaceous chondrites NWA 801 (CR), Leoville (CV3.1), Paris (CM2.9), Maribo (CM2.8) and Bells (CM-an). We observe a predominant and constant sub-solar Co/Ni ratio of CR, CM and CM-an metal grains. In Ni versus Co space, the metal grains fall below modelled curves for equilibrium condensation of metals from a solar gas. From Ni versus Cr plots, we infer that Paris (and possibly Leoville) metal grains could have maintained a primary condensation signature, although for most grains, condensation must have occurred under disequilibrium conditions. CR and isolated CM-an metals mostly fall outside of the predicted condensation fields. Based on metal-silicate partition coefficients of Ni and Co that vary with pressure, we interpret their Co/Ni signatures as having a planetary origin, with presumable extraction by impact jetting. Considering that almost all CM and CR metal grains have the same Co/Ni ratio, we cannot rule out a planetary origin for CM metal grains. We relate the highly siderophile element (HSE) patterns of carbonaceous chondrite metal to mixing and subsequent equilibration of refractory metal nuggets (RMN), FeNi alloys and silicate chondrule precursors. As with the Co/Ni ratios, the HSE patterns of CM, CM-an, CR and CV metal grains are nearly identical, suggesting that the abundance and nature of the metal precursor materials were similar for carbonaceous chondrites. The overall volatility patterns of CV, CM and CR chondrites, suggest that the latter form under more oxidizing conditions than CV chondrites. The volatility patterns of Paris metal grains overlap with CV and CR chondrule metals, implying variable P-T-fO_2 conditions during CM chondrule formation. Finally, we comment on the origin of metal grains in various petrological settings. Chondrule rim and isolated metal grains are likely derived and expelled from the equilibrated core metal and were subsequently altered to include and re-equilibrate with materials from the disk. Trace element analyses of the anomalous CM chondrite Bells metal grains show potential relationships with CM chondrite and CH chondrite metal for the chondrule cores and isolated grains, respectively. Small metal grains from CM chondrite Maribo, which are located in the chondrite matrix, potentially have distinct volatility patterns from CR and Paris isolated grains, hinting at a distinct origin for small metal grains and large chondrule-derived metal. Future work on carbonaceous chondrite metal should include an investigation of small (micron scale) versus large isolated metal grains.
© 2022 The Authors. Published by Elsevier Ltd. This is an open access article under the CC BY license (http://creativecommons.org/licenses/by/4.0/).

Keywords: Metal; Chondrites; Chondrule formation; LA-ICPMS

* Corresponding author at: Center for Star and Planet Formation, Globe Institute, University of Copenhagen, Øster Voldgade 5-7, 1350 Copenhagen, Denmark.
E-mail address: elishevah.vankooten@sund.ku.dk (E.M.M.E. van Kooten).

https://doi.org/10.1016/j.gca.2022.01.008
0016-7037/© 2022 The Authors. Published by Elsevier Ltd.
This is an open access article under the CC BY license (http://creativecommons.org/licenses/by/4.0/).

1. INTRODUCTION

Unraveling the early Solar System's dynamic evolution of planet formation within the gaseous protoplanetary disk can be approached from a cosmochemical perspective by looking at chondrites, which represent the most primitive building blocks of the planets. Chondrites are suggested to reflect a wide range of planetary reservoirs, including the terrestrial (e.g. ordinary and enstatite chondrites), the gas giant (e.g. carbonaceous chondrites; Kruijer et al., 2017; Warren, 2011) and potentially the cometary accretion regions (e.g. metal-rich carbonaceous chondrites; van Kooten et al., 2016). They are recognized and classified by their chondrule inventory (i.e., size, texture, composition of once molten silicate droplets that formed during transient heating events in the disk), the presence of refractory calcium-aluminum-inclusions (CAIs), which represent the first condensates of the cooling protoplanetary disk, and the interstitial fine-grained dust (matrix) (Scott and Krot, 2014). Together, these chondritic components are probed for their origins and subsequent transport in the disk using chemical and isotopic analyses.

Other important but often overlooked constituents of the chondritic inventory are FeNi metals that are present in varying abundances within chondrites (<5 vol.% in carbonaceous chondrites to <70 vol.% in metal-rich carbonaceous chondrites, (Scott and Krot, 2014)) and are contained within chondrule interiors, as part of the chondrule rims and as isolated grains in the matrix. Determining the detailed compositions of these metals is critical to understand (1) the processes and thermodynamical conditions of chondrule formation, (2) condensation processes in the protoplanetary disk and (3) the redistribution of elements within a chondrite during the early onset of secondary alteration. Even though metal is a key component of chondrules and chondrites, its composition has not been studied nearly as well as the silicate portion of chondrites.

The petrology and composition of chondritic metals has been intermittently investigated during the past decades. Most of these studies are limited to enstatite chondrites (Kadlag et al., 2019; Kimura, 1988; Lehner et al., 2010; Lin and Goresy, 2002), ordinary chondrites (Grossman and Wasson, 1985; Kong and Ebihara, 1997; Humayun and Campbell, 2002; Okabayashi et al., 2019; Gilmour and Herd, 2020) and metal-rich carbonaceous chondrites (Lee et al., 1992; Meibom et al., 1999; Campbell et al., 2001; Connolly et al., 2001; Campbell and Humayun, 2004; Wasson and Rubin, 2010; Humayun, 2012; Jacquet et al., 2013; Nakanishi et al., 2021), in which the metal grains are abundant, mostly unaffected by secondary alteration and sufficiently large for elemental analyses. The metal compositions of carbonaceous CM and CV chondrites remain largely unexplored (Grossman et al., 1979; Zanda et al., 1994; Bourot-Denism et al., 2010; Kimura et al., 2011; Hewins et al., 2014) even though these chondrites are among the most abundant and typical carbonaceous chondrites. The known chemical composition is limited to the most abundant elements that are readily analyzed by electron microprobe (EMP) (i.e., Fe, Ni, Co, Cr, Si and P). Nevertheless, siderophile and chalcophile trace elements that may be present in chondritic metals may possess a wealth of information due to their wide range of cosmochemical properties. For example, the siderophile nature of some elements depends on the thermodynamical conditions in which the metal formed, and the different volatilities of these elements can shed light on the formation processes of metals. This way, the trace element compositions of carbonaceous chondrite metals can constrain the nature of the metal precursors as well as the condensation, evaporation and metal-silicate equilibration processes related to thermal processing in the solar nebula and during chondrule formation. Indeed, there is still considerable debate on whether chondritic metals reflect the composition of their precursors, or if they further equilibrated with silicate melts and/or nebular gas during chondrule formation. In this study, we use Co/Ni and Cr/Ni ratios, HSE and overall volatility patterns of carbonaceous chondrite metal to constrain the origin of these metals and subsequent processing of this phase in the protoplanetary disk and during chondrule formation. Furthermore, we use these analyses to constrain whether the metals in various petrological settings (i.e., chondrule cores, rims and isolated metal from the matrix) are related to each other. Finally, metal is considered as a carrier of nucleosynthetic and stable isotopes that trace precursor materials and volatile-related processes, such as Mo, W (Budde et al., 2016a) and Zn (Pringle et al., 2017; van Kooten and Moynier, 2019), respectively. Detailed knowledge of the chondritic metal composition can help to establish the total mass balance of siderophile element contributions to the isotopic signature of chondritic components such as chondrules and matrix.

Here, we report on the major and trace element composition of CR, CV and CM chondrite metals from different petrological settings, including the chondrule interiors, rims and isolated grains located in the matrix. Based on these data, we discuss (1) the effect of secondary alteration on metal compositions, (2) the constraints that minor and trace element signatures place on metal precursor materials and subsequent modifications of metal compositions in the protoplanetary disk and during chondrule formation and, finally, (3) implications from chondrule metal compositions on the physicochemical conditions of chondrule formation.

2. MATERIALS AND METHODS

2.1. Samples

We have selected samples with relatively low degrees of secondary alteration from various carbonaceous chondrite groups, since metal is the first mineral phase to oxidize and/or exsolve during secondary alteration on the chondrite parent bodies (Pignatelli et al., 2017). To this end, we have chosen NWA 801 (CR2.8, 3 thick sections; (Harju et al., 2014)), Leoville (CV3.1, 3 thick sections; (Bonal et al., 2006)), Paris (CM2.9, 1 thick section; (Rubin et al., 2007)), Maribo (CM > 2.8, 1 thick section; (Rubin et al., 2007)) and Bells (CM2.2-an, 1 thick section; (Rubin et al., 2007)). From these chondrites, chondrule interior and rim grains were analyzed, along with multiple isolated grains from the matrix.

In detail, NWA 801 is a CR chondrite that underwent a negligible amount of thermal metamorphism and aqueous alteration (van Kooten et al., 2019). The chondrite likely underwent some terrestrial weathering as evidenced by the oxidation of metal grain rims and the presence of Fe-rich cracks and veins. These areas were avoided during the selection of metal grains.

Paris and Maribo represent the most unaltered CM chondrites in our collection (Haack et al., 2012; Hewins et al., 2014; van Kooten et al., 2018, 2019). Even so, these chondrites are very different with respect to i.e. their organic structure, the hydrogen isotope composition of the matrix and the abundance of metal (van Kooten et al., 2018). In detail, in its most unaltered areas, Paris contains up to 5 wt.% metal (Hewins et al., 2014), whereas Maribo contains <1 wt.% metal (van Kooten et al., 2018). However, Maribo does contain a significant amount of small nm-sized metal grains that are contained in the fine-grained matrix and are observed by transmission electron microscope (van Kooten et al., 2018), which could amount to the same metal abundance as Paris. The total metal abundance of Paris is estimated from larger metal grains (<500 μm diameter) that can be recognized by EMP.

Bells is classified as an anomalous CM chondrite that underwent a significant degree of aqueous alteration (Brearley, 1995; Kallemeyn, 1995; Mittlefehldt, 2002). Nevertheless, it contains abundant metal grains, within and outside of chondrules (van Kooten et al., 2018). This chondrite can best be defined as an intermediate composition between CM and CR chondrites (van Kooten et al., 2020).

The Leoville CV chondrite is one of the most unaltered chondrites within this group, even though it underwent some degree of thermal metamorphism. Its petrology and composition are described in detail by van Kooten et al. (2019).

2.2. SEM imagining and microprobe analyses of standards and samples

All standards and samples were imaged by Zeiss EVO MA10 scanning electron microscope at IPGP, resulting in high resolution BSE images. This allowed for the selection of chondritic metal grains unaltered by secondary alteration and the determination of standard homogeneity. Subsequently, standards and samples were transferred to the Cameca SX-100 electron microprobe (EMP) at the Centre de Microanalyse de Paris VI (CAMPARIS) and were analyzed using well-characterized mineral standards. An accelerating voltage of 15 keV and a beam current of 10 nA were used and the counting times were 10–20 s for major elements and 20–90 s for trace elements. Rasters of 30 μm were made on both chondritic metal grains and metal reference standards.

2.3. LA-ICPMS analyses of standards and samples

Laser ablation ICPMS analyses were carried out at the Geological Survey of Denmark and Greenland (GEUS). Carbon coatings were removed with ethanol from the thick sections before analysis. A NWR213 frequency-quintupled solid state Nd:YAG laser system from Elemental Scientific Lasers, mounted with a TV2 ablation cell was coupled to an Element 2 double-focusing single-collector magnetic sector-field ICPMS from Thermo-Fisher Scientific. The laser was heated for at least 15 minutes before operation to ensure a stable laser output energy. The plasma of the ICPMS was lit minimum an hour before run time to stabilize the background signal. After cleaning, the samples were inserted into the ablation cell, which was flushed several times with the helium carrier gas to reduce the gas blank level. Data were acquired from single spot analysis of 40 (session 1) and 25 μm (session 2), using a nominal laser fluence of ~10 J/cm^2 and a pulse rate of 10 Hz. The total acquisition time for a single analysis was approximately two minutes, including 30 s gas blank measurement followed by laser ablation for 60 s and washout for 20 s. All samples were measured using a standard-sample bracketing technique, where 8 individual sample analyses were alternated with repeats of three synthesized metal standards and the Santa Clara iron meteorite. The production by piston cylinder experiments and wet-chemistry analyses of the metal standards is described in detail in Appendix A. Together, these standards encompass a range of elements and their concentrations expected in chondritic metals. The Santa Clara meteorite is a highly homogeneous IVB iron and, hence, suitable to use as reference standard (Campbell and Humayun, 2005). Before sample analyses, an entire analytical session of ~12 hours was dedicated to measuring the standards and tuning instrument parameters to optimize measurement conditions. The following isotopes were analyzed during all sessions: ^{51}V, ^{53}Cr, ^{55}Mn, ^{57}Fe, ^{59}Co, ^{65}Cu, ^{66}Zn, ^{95}Mo, ^{101}Ru, ^{103}Rh, ^{108}Pd, ^{120}Sn, ^{182}W, ^{189}Os, ^{193}Ir, ^{195}Pt and ^{197}Au. Note that Re, also a HSE, was not measured here due to the lack of an appropriate standard during the synthesizing of the experimental metals. Co was used as the internal standard element, since Ni cones were used by the ICPMS. Data reduction was performed off-line through the Iolite v.2.5 software and the trace element data reduction scheme (Paton et al., 2011). The limit of detection (LOD) was calculated using the 3-sigma deviation of the blanks. The quality of the data was checked by alternating the synthesized metals employed as the external standard matrix in Iolite to assess which standard yielded the most accurate and precise results (Fig. S2, Appendix A). Overall, E363 and E391 provide the most accurate values for all elements. Standard E383 has relatively low concentrations of PGE (<200 ppb), which results in overestimations of PGE in the other standards (≫1 ppm). Using E363 and E391, the 2SE% uncertainties of the reference standards (E363, E391, E383 and Santa Clara) are typically <4% for concentrations >1 ppm. Sub-ppm concentrations have larger errors, especially if their detection limits are relatively high (e.g., Zn and Sn, ~300 and ~200 ppb LOD, respectively). For example, the V, Zn and Sn concentrations of the Santa Clara meteorite are found to be 0.10 ± 0.02 ppm (19 2SE %), 0.22 ± 0.05 ppm (21 2SE%) and 0.09 ± 0.06 ppm (65 2SE%), respectively (using E391 as standard). Zinc, Rh, Sn, W and Au have concentrations in the sub-ppm range for the chondrite metal grains analyzed here. Of these

elements, Rh, Au and W all have concentrations above the calculated LOD (~10 ppb). Collectively, for most elements we estimate a 2SE error of <4 % and for sub-ppm concentrations above the LOD, <21%. Note that this error does not include the uncertainty on the ICP-Q-MS and HR-ICPMS analyses of the synthesized metal standards (see Appendix A). For all LA-ICPMS data reported below, we reference against the E363 standard.

3. RESULTS

3.1. Petrography of CR, CM and CV chondritic metals

3.1.1. NWA 801 (CR)

In this study, we have investigated the petrography and composition of CR metal grains in three different settings: four chondrule cores, four chondrule rims (of which two correspond to the chondrule cores) and four are isolated metal grains. The grains were imaged in BSE mode at high-contrast, low luminosity settings to highlight inclusions and the difference between Ni-poor (kamacite) and Ni-rich regions (taenite) within the metal grains (Figs. 1 and S5). The determination of such variations is important to assess the degree of thermal metamorphism (Kimura et al., 2011) as well as the heterogeneity of each grain with respect to the following LA-ICPMS analyses. The quality of these analyses is partially dependent on the internal normalization of the measurement using Co.

In Fig. 1, we show the BSE images of representative core, rim and isolated metal grains from sections of NWA 801. We found that within this CR chondrite, the texture of the grains, independent of their setting, is very uniform and no distinct differences could be observed between the grains. Although some compositional heterogeneity appears to be present within the grains, the variation is minor as evidenced by EMP analyses (see Section 3.2). Plessitic intergrowths, as observed by Jacquet et al. (2013) are not found in our sections of NWA 801, although the (in BSE mode) black Cr- and P-rich inclusions observed within the grains are consistent with observations by these authors. Most grains are characterized by well-rounded, spherical or elliptical shapes. Irregularities around the boundaries are related to oxidation from secondary alteration during terrestrial weathering (see section 4.1).

3.1.2. Paris and Maribo (CM > 2.8)

We report on the petrology and composition of CM metal grains that are located in chondrule cores ($n = 7$), rims ($n = 4$) and as isolated grains ($n = 9$). We note that for some grains it is difficult to determine if they are core, rim or isolated grains (Table 1) due to the cut of the thick section. Many grains that appear as isolated grains have small silicate rims surrounding them, suggesting they are in fact chondrule core or rim metals. As noted in Section 2.1, Maribo contains less metal relative to Paris on the micrometer-millimeter scale. The size of Paris metal is similar to the range found in CR chondrites, typically a few hundred micrometers.

In Fig. 2, we show the BSE images of representative core, rim and isolated metal grains from the Paris and Maribo section (see also Fig. S6). Most grains appear compositionally homogeneous and do not contain any significant exsolution features. There are sparse Cr- and P-rich inclusions (black in Fig. 2) and most grains are well-rounded. Euhedral precipitates of silica, as mentioned by Hewins et al. (2014) are not observed in the metal. We have investigated one exceptional grain (Fig. 2B), with clear kamacite-taenite exsolutions and abundant black inclusions. We note that even though Maribo metal is less abundant on the micrometer-millimeter scale, the petrology of the grains is indistinguishable from the Paris metal.

3.1.3. Bells (anomalous CM2.2)

We have studied seven isolated grains and three chondrule cores of the Bells anomalous CM chondrite (Figs. 3 and S7). The composition of the rim grains was not investigated due to their small size. Typically, the metal grains in Bells are an order of magnitude smaller than those observed in Paris (<50 μm) and more similar in size to the Maribo metal grains. The shape of the grains is also more variable than seen in Paris, and often square grains are observed. In Fig. 3, we show representative grains of Bells' core and isolated metal. Most grains have abundant black (Cr- and P-rich inclusions), which are round to elongated in shape. Some rare micron-sized Ni-rich inclusions also are observed.

3.1.4. Leoville (CV3.1)

We have investigated the metal grains of four chondrule cores, four chondrule rims (for their metal and complementary sulfides) and two isolated grains (Figs. 4 and S8). The size of the Leoville metal (<100 μm) is typically smaller than Paris or CR chondritic metal, but larger than Bells or Maribo. The grains are often elongated, which is likely the result of shear strain and foliation of the Leoville meteorite (Martin et al., 1975). In Fig. 4, we show representative core, rim and isolated grains from Leoville. While mostly martensitic, many metal grains contain exsolutions of kamacite and taenite (<30 μm). In addition, Cr- and P-rich and rare silica-rich inclusions are observed.

3.2. Electron microprobe analyses

Table presents Fe, Ni, S, P, Co, Cr, Cu and Si concentrations for metal grains from the CR, CM, CM-an and CV chondrites. The data reflect averaged concentrations from multiple raster analyses in one of three petrological settings (i.e. core, rim and isolated metal, see Table 1 for further explanation and Table S3 for individual data points). Results on S, P, Cr, Cu and Si are presented in Appendix B.

3.2.1. Ni versus Co

The Ni and Co concentrations of CR, CM and CM-an metal form a positive correlation that deviates from the solar (CI chondrite) trend (Fig. 5). This sub-chondritic correlation is well-defined for each representative of the aforementioned chondrite groups (NWA801, Paris, Maribo and

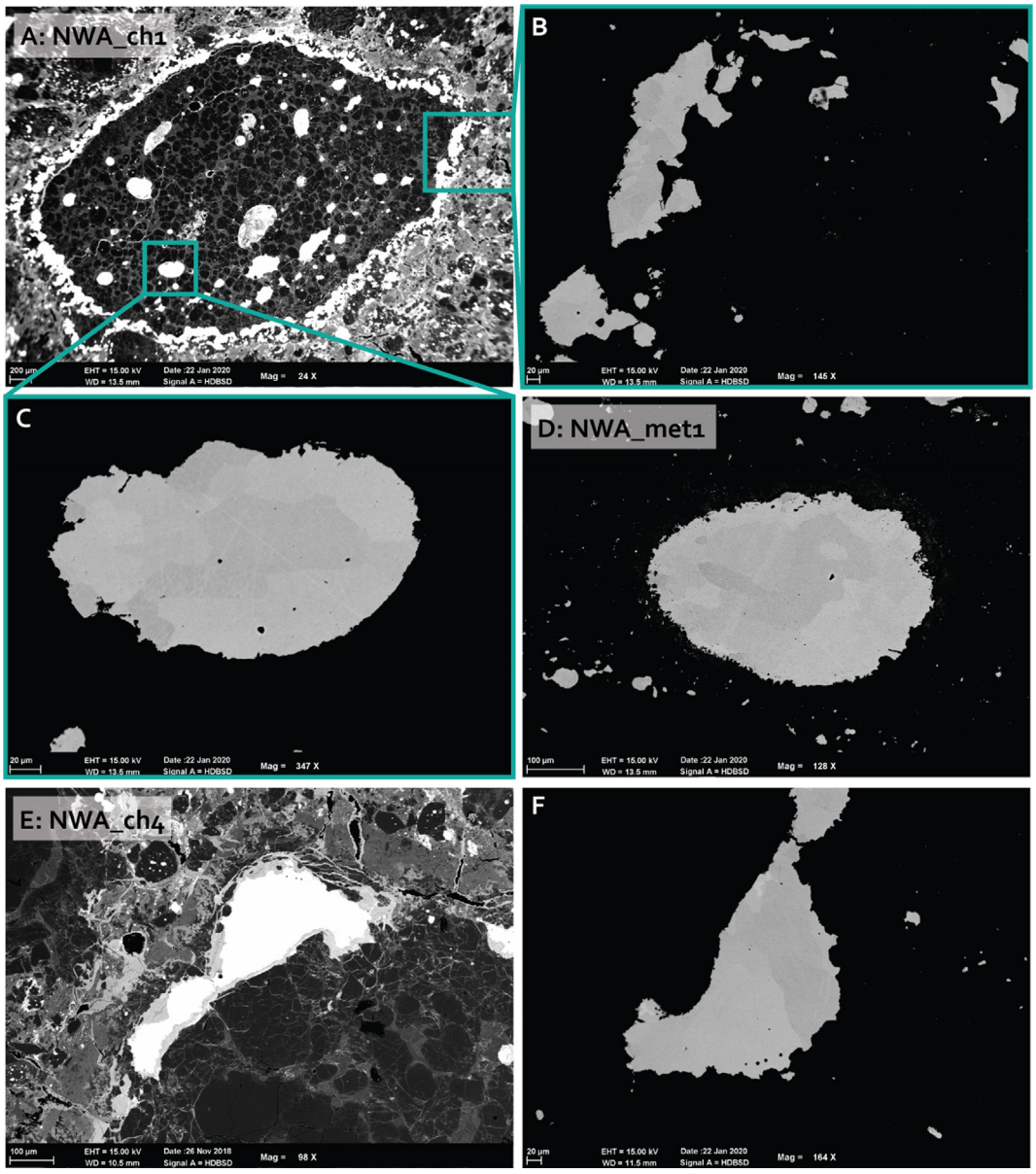


Fig. 1. Back scattered electron images of representative NWA801 CR chondrite metal grains. B and C are zoom-ins of A: NWA_ch1. Metal grains are shown with increased contrast (B, C, D, F) to highlight compositional zoning of Ni-poor (kamacite) and Ni-rich (taenite) regions. High resolution BSE images of all NWA801 metal grains used in this study can be found in Fig. S5.

Bells) and holds true for individual as well as averaged raster analyses. Metal from CR and CM chondrites have overlapping Ni and Co concentrations, whereas metal from Bells also has higher Ni and Co concentrations (Fig. 5C). The metal from one Paris chondrule (ch5) falls on the solar line (Fig. 5A and B). This chondrule is different from the other chondrules and consists completely of a metal core, with large kamacite-taenite exsolutions and Si, Cr and P inclusions. Previous EMP analyses of Ni and Co in CM and CR chondrite metal (Connolly et al., 2001; Wasson and Rubin, 2010; Kimura et al., 2011; Jacquet et al., 2013; Hewins et al., 2014) were done using single-point analyses (<10 μm beam diameter) and resulted in a scatter plot averaging around the solar line (Fig. 5A and B). While this has been interpreted as chondrite metal having a solar Co/Ni ratio, these data cannot resolve a solar from a subchondritic Co/Ni ratio, although metal grains with high Ni contents have been pointed out to deviate from the solar line (Wasson and Rubin, 2010; Jacquet et al., 2013). Single point, in contrast to raster analyses that sample a larger area of the metal, will result in more heterogeneous compositions and scatter of the data. The averaged single points may not represent the bulk composition of a metal grain as well as the rasters used in this study. This is reflected by the more extreme case of Leoville metal, which contains larger exsolutions and shows distinct trends of Ni-rich and Ni-poor data moving away from the solar Co/Ni ratio (Fig. 5D). One averaged datapoint, reflecting all metal

Table 1
Electron microprobe data from CR, CM, CM-an and CV chondrite metal grains in wt.%. C = core, R = rim, met = metal, sf = sulfide and IG = isolated grain. B.d. = below detection limit and n. a. = not analyzed. The light grey numbers are the corresponding 2SD standard deviations from multiple raster analyses, where n depicts the number of rasters. A single row represents multiple rasters and grains within the same petrological setting. For example, Paris ch15 R ($n = 3$) means 3 raster analyses in one or more grains in the metal rim of chondrule 15. Where the number of rasters amounts to <2, note that the SD value is statistically meaningless, but gives an indication of the variation. For individual analyses and images of the grains and petrological settings, see Supplementary Tables S3 and S4 and Figs. S1–S4, where individual sample analyses can be directly compared to SEM images of the metal grains. Note that, except for NWA 801, none of the core and rim metals belong to the same chondrule. In NWA 801, the cores and rims belonging to the same chondrule also have the same name (f.e. NWA2_ch1). The literature data is from Jacquet et al. (2013) in blue and Wasson and Rubin (2010) in yellow for CR chondrites. Note that Wasson and Rubin (2010) also have data for Fe, Ni and Co, but these data have a larger error. The literature data from Leoville core metal is from Zanda et al. (1994) and that from Paris is data from Hewins et al. (2014).

CR	Setting	n	S		Fe		Ni		P		Cr		Co		Cu		Si		Total
NWA1_ch1	R	10	b.d.		92.4	2.4	6.0	1.2	0.29	0.11	0.26	0.02	0.25	0.04	b.d.		b.d.		99.1
NWA1_ch2	R	9	b.d.		93.8	1.6	5.1	0.6	0.13	0.04	0.49	0.03	0.21	0.02	b.d.		b.d.		99.7
NWA1_ch4	R	6	b.d.		94.8	1.2	4.9	0.3	0.19	0.07	0.36	0.02	0.21	0.01	b.d.		b.d.		100.5
NWA2_ch1	R	6	b.d.		94.0	1.6	5.6	0.3	0.33	0.07	0.37	0.03	0.22	0.02	b.d.		b.d.		100.4
NWA1_ch3	C	3	b.d.		90.9	0.8	7.7	0.2	0.33	0.03	0.25	0.04	0.30	0.01	b.d.		b.d.		99.5
NWA2_ch1	C	6	b.d.		92.0	2.2	6.9	0.4	0.23	0.04	0.33	0.01	0.28	0.02	b.d.		b.d.		99.6
NWA2_met1	C	2	b.d.		90.5	0.5	7.1	0.2	0.50	0.06	0.26	0.01	0.27	0.00	0.008	0.002	b.d.		98.6
NWA2_ch2	C	4	b.d.		92.1	1.5	7.3	0.2	0.19	0.07	0.32	0.00	0.27	0.02	b.d.		b.d.		100.2
NWA1_met1	IG	5	b.d.		93.9	1.3	5.2	0.2	0.23	0.05	0.18	0.02	0.21	0.01	b.d.		b.d.		99.6
NWA1_met1	IG	2	b.d.		93.3	0.9	5.0	0.1	0.37	0.05	0.37	0.02	0.21	0.01	b.d.		b.d.		99.2
NWA1_met2	IG	3	b.d.		93.1	1.1	5.2	0.2	0.23	0.02	0.29	0.02	0.21	0.01	b.d.		0.037	0.088	99.0
NWA2_met1	IG	4	b.d.		94.5	0.9	5.2	0.2	0.15	0.09	0.14	0.01	0.21	0.01	b.d.		b.d.		100.2
Average	**R**	4	***b.d.***		***93.7***	*2.1*	***5.4***	*1.0*	***0.24***	*0.19*	***0.37***	*0.19*	***0.22***	*0.03*	***b.d.***		***b.d.***		
	C	4	***b.d.***		***91.4***	*1.5*	***7.3***	*0.7*	***0.31***	*0.28*	***0.29***	*0.08*	***0.28***	*0.03*	***<0.008***		***b.d.***		
	IG	4	***b.d.***		***93.7***	*1.3*	***5.1***	*0.2*	***0.25***	*0.18*	***0.24***	*0.22*	***0.21***	*0.00*	***b.d.***		***<0.037***		
Literature	**R**		*n.a.*		***94.5***	*0.6*	***5.4***	*0.6*	***0.16***	*0.03*	***0.29***	*0.15*	***0.25***	*0.02*	***0.007***	*0.001*	*n.a.*		
	C		*n.a.*		***92.8***	*1.0*	***6.9***	*0.9*	***0.17***	*0.03*	***0.21***	*0.09*	***0.31***	*0.02*	***0.005***	*0.000*	*n.a.*		
	IG		*n.a.*		***94.5***	*0.3*	***5.5***	*0.2*	***0.16***	*0.04*	n.a.		***0.26***	*0.01*	***0.004***	*0.001*	*n.a.*		
CV																			
LeoB_ch1	C	6	b.d.		94.0	2.5	5.0	1.2	b.d.		0.26	0.44	0.29	0.13	b.d.		b.d.		99.5
LeoB_ch3	C	6	b.d.		91.2	7.2	6.9	7.8	b.d.		0.74	0.12	0.34	0.17	0.024	0.053	0.046	0.058	99.2
Leo C1	C	9	0.06	0.16	91.7	5.0	5.8	3.0	b.d.		0.36	0.64	0.32	0.18	0.008	0.012	b.d.		98.2
Leo C5	C	3	b.d.		94.0	n.a.	4.4	n.a.	b.d.		0.55	n.a.	0.40	n.a.	0.011	n.a.	b.d.		99.5
Leo C5	R-met	6	1.81	8.63	86.2	13.9	8.7	13.8	b.d.		0.58	0.17	0.30	0.17	0.035	0.086	0.042	0.055	97.6
LeoB_ch2	R-met	3	b.d.		93.5	0.5	4.7	0.2	b.d.		0.52	0.05	0.45	0.02	0.006	0.001	0.052	0.031	99.2
LeoB_met1	R-met	2	0.13	0.29	86.6	14.8	9.9	14.0	b.d.		0.64	0.17	0.41	0.15	0.037	0.091	0.049	0.038	97.6
LeoB_ch4	R-met	6	0.08	0.06	90.3	2.9	5.5	0.8	b.d.		0.64	0.10	0.46	0.02	0.010	0.004	0.149	0.291	97.1
LeoB_met1	R-sf/met	2	18.59	9.82	68.3	19.4	9.1	14.3	b.d.		0.79	0.06	0.16	0.23	0.056	0.064	0.045	0.021	96.9
LeoB_ch2	R-sf	2	33.71	0.65	63.6	2.0	b.d.		b.d.		b.d.		b.d.		0.006	0.001	b.d.		97.4
LeoB_ch3	R-sf	2	34.06	0.41	63.5	0.6	b.d.		b.d.		b.d.		b.d.		b.d.		b.d.		97.6
Leo2_ch1	R-sf	7	34.06	0.59	63.5	1.6	0.3	0.6	b.d.		b.d.		0.02	0.02	b.d.		b.d.		97.9
LeoB_met1	IG	2	b.d		92.9	3.8	6.2	0.3	b.d.		0.01	0.01	0.67	0.03	0.006	0.001	b.d.		99.7

LeoB_met2	IG	3	b.d.		81.8	30.8	18.5	30.5	b.d.		0.01	0.01	0.77	0.51	0.078	0.194	b.d.		100.9
Average	**R-met**	3	***<0.13***		***90.1***	*6.9*	***6.7***	*5.6*	***b.d.***		***0.60***	*0.14*	***0.44***	*0.05*	***0.017***	*0.035*	***0.083***	*0.115*	
	R-sf	3	***33.95***	*0.40*	***63.5***	*0.2*	***<0.3***		***b.d.***		***<0.004***		***<0.02***		***<0.006***		***b.d.***		
	C	4	***<0.09***		***92.7***	*3.0*	***5.5***	*2.1*	***b.d.***		***0.48***	*0.42*	***0.34***	*0.10*	***0.014***	*0.017*	***<0.046***		
	IG	2	***b.d.***		***87.3***	*15.7*	***12.3***	*17.3*	***b.d.***		***0.01***	*0.00*	***0.72***	*0.14*	***0.042***	*0.101*	***b.d.***		
Literature	**C**						***4.8***	*0.3*	***<0.02–0.79***		***0.49***	*0.63*					***<0.02–0.07***		
CM-an																			
Bells met3	IG	3	0.11	0.07	84.1	0.8	10.4	0.2	0.05	0.00	0.24	0.00	0.38	0.00	b.d.		b.d.		95.1
Bells met4	IG	4	0.09	0.18	81.9	2.9	9.6	1.8	0.09	0.01	0.13	0.01	0.35	0.04	0.011	0.006	b.d.		92.1
Bells met5	IG	2	b.d.		83.6	1.6	8.9	0.5	0.09	0.01	0.29	0.00	0.34	0.01	b.d.		b.d.		93.2
Bells met6	IG	2	b.d.		84.7	1.7	8.1	0.9	0.08	0.01	0.21	0.03	0.31	0.05	b.d.		b.d.		93.3
Bells met7	IG	2	b.d.		86.6	4.9	6.8	6.1	0.21	0.36	0.48	0.72	0.27	0.18	b.d.		0.15	0.29	94.4
Bells met8	IG	2	b.d.		90.5	n.a.	6.2	n.a.	0.14	n.a.	0.29	n.a.	0.26	n.a.	b.d.		b.d.		97.4
Bells met1	IG/C?	2	0.06	n.a.	93.3	n.a.	4.9	n.a.	0.28	n.a.	0.11	n.a.	0.22	n.a.	0.009	n.a.	b.d.		98.7
Bells met2	C	3	0.13	n.a.	91.7	n.a.	3.6	n.a.	0.21	n.a.	0.13	n.a.	0.16	n.a.	0.025	n.a.	b.d.		95.9
Bells ch1	C	1	0.06	n.a.	84.2	n.a.	5.5	n.a.	0.11	n.a.	0.06	n.a.	0.23	n.a.	0.030	n.a.	0.29	n.a.	90.5
Bells ch2	C	2	b.d.		89.0	n.a.	5.0	n.a.	0.30	n.a.	0.68	n.a.	0.21	n.a.	0.009	n.a.	b.d.		95.2
Average	**IG**	3	***<0.114***		***85.2***	*6.0*	***8.3***	*3.2*	***0.11***	*0.11*	***0.27***	*0.23*	***0.32***	*0.10*	***<0.011***		***<0.15***		
	C	6	***<0.127***		***88.3***	*7.6*	***4.7***	*2.0*	***0.21***	*0.19*	***0.29***	*0.68*	***0.20***	*0.07*	***0.021***	*0.021*	***<0.29***		
CM																			
Maribo met1	IG	1	0.09	n.a.	95.6	n.a.	5.3	n.a.	0.26	n.a.	0.27	n.a.	0.21	n.a.	0.041	n.a.	0.04	n.a.	101.7
Maribo met2	IG	1	0.07	n.a.	90.0	n.a.	4.5	n.a.	0.27	n.a.	0.12	n.a.	0.20	n.a.	0.038	n.a.	0.91	n.a.	96.1
Maribo met3	IG	1	0.05	n.a.	89.5	n.a.	5.1	n.a.	0.18	n.a.	0.08	n.a.	0.21	n.a.	0.033	n.a.	0.18	n.a.	95.3
Maribo met4	IG	1	0.08	n.a.	92.0	n.a.	4.8	n.a.	0.21	n.a.	0.07	n.a.	0.20	n.a.	0.032	n.a.	0.42	n.a.	97.8
Average	**IG**	4	***0.07***	*0.04*	***91.8***	*5.5*	***4.9***	*0.6*	***0.23***	*0.09*	***0.13***	*0.19*	***0.20***	*0.01*	***0.036***	*0.008*	***0.38***	*0.76*	
Paris ch1	IG	2	b.d.		93.0	n.a.	4.7	n.a.	0.32	n.a.	0.84	n.a.	0.20	n.a.	0.010	n.a.	0.06	n.a.	99.1
Paris ch6	C?	5	b.d.		93.9	1.9	4.8	0.4	0.42	0.09	0.67	0.04	0.21	0.02	b.d.		0.07	0.09	100.1
Paris ch8	C?	6	b.d.		94.5	2.0	5.2	0.1	0.26	0.00	0.56	0.02	0.22	0.00	b.d.		0.08	0.02	100.7
Paris ch10	C?	3	b.d.		92.7	2.4	5.2	0.2	0.47	0.00	0.72	0.01	0.23	0.01	0.007	0.007	0.11	0.03	99.4
Paris ch14	C?	5	b.d.		92.9	3.0	6.7	0.4	0.39	0.01	0.58	0.00	0.27	0.01	b.d.		0.05	0.01	100.8
Paris ch2	C	1	b.d.		91.7	3.1	5.5	0.1	0.42	0.00	0.47	0.01	0.23	0.01	b.d.		0.12	0.05	98.3
Paris ch5	C	5	b.d.		91.7	0.1	7.1	0.0	0.34	0.00	0.48	0.02	0.35	0.00	0.014	0.003	0.51	0.04	100.3
Paris ch7	C	2	b.d.		92.8	0.7	5.8	0.3	0.39	0.00	0.66	0.01	0.24	0.01	0.009	0.001	0.05	0.05	99.9
Paris ch9	C	5	b.d.		93.0	1.5	5.6	0.3	0.38	0.00	0.50	0.03	0.23	0.01	b.d.		b.d.		99.6
Paris ch11	C	2	b.d.		92.0	1.9	6.9	0.4	0.15	0.00	0.06	0.06	0.27	0.02	0.007	0.006	b.d.		99.3
Paris ch12	C	4	b.d.		92.8	0.6	6.2	0.9	0.15	0.08	0.84	0.06	0.26	0.01	b.d.		0.75	0.05	100.9
Paris ch16	C	2	b.d.		92.9	2.1	4.6	0.2	0.38	0.01	0.71	0.05	0.19	0.01	0.024	0.004	b.d.		98.8
Paris ch13	C/R?	3	b.d.		94.9	0.3	5.0	0.0	0.49	0.00	0.46	0.02	0.21	0.00	b.d.		b.d.		101.0
Paris ch3	C/R?	4	b.d.		92.0	2.3	5.2	1.0	0.40	0.07	0.94	0.04	0.22	0.00	b.d.		0.92	0.07	99.6

Paris ch4	R	2	b.d.		92.3	n.a.	4.5	n.a.	0.34	n.a.	0.73	n.a.	0.20	n.a.	b.d.		0.05	n.a.	98.0
Paris ch15	R	3	b.d.		90.8	0.8	4.7	0.6	0.15	0.07	1.10	0.16	0.21	0.03	0.008	0.008	1.21	0.06	98.2
Average	**R**	2	b.d.		***91.5***	*2.1*	***4.6***	*0.3*	***0.24***	*0.28*	***0.92***	*0.53*	***0.20***	*0.02*	***<0.008***		***0.63***	*1.65*	
	C	7	b.d.		***92.4***	*1.2*	***5.9***	*1.7*	***0.31***	*0.23*	***0.53***	*0.50*	***0.25***	*0.10*	***<0.024***		***<0.36***		
	IG	1	b.d.		***93.0***		***4.7***		***0.32***		***0.84***		***0.20***		***0.010***		***0.06***		
	C/R		***0.07***	*0.07*	***92.7***	*2.9*	***5.7***	*2.6*	***0.44***	*0.55*	***0.48***	*0.81*	***0.26***	*0.26*			***0.27***	*0.30*	
Literature	**IG**		***0.04***	*0.26*	***93.8***	*3.7*	***5.6***	*2.0*	***0.43***	*0.47*	***0.59***	*0.73*	***0.25***	*0.29*			***0.11***	*1.40*	

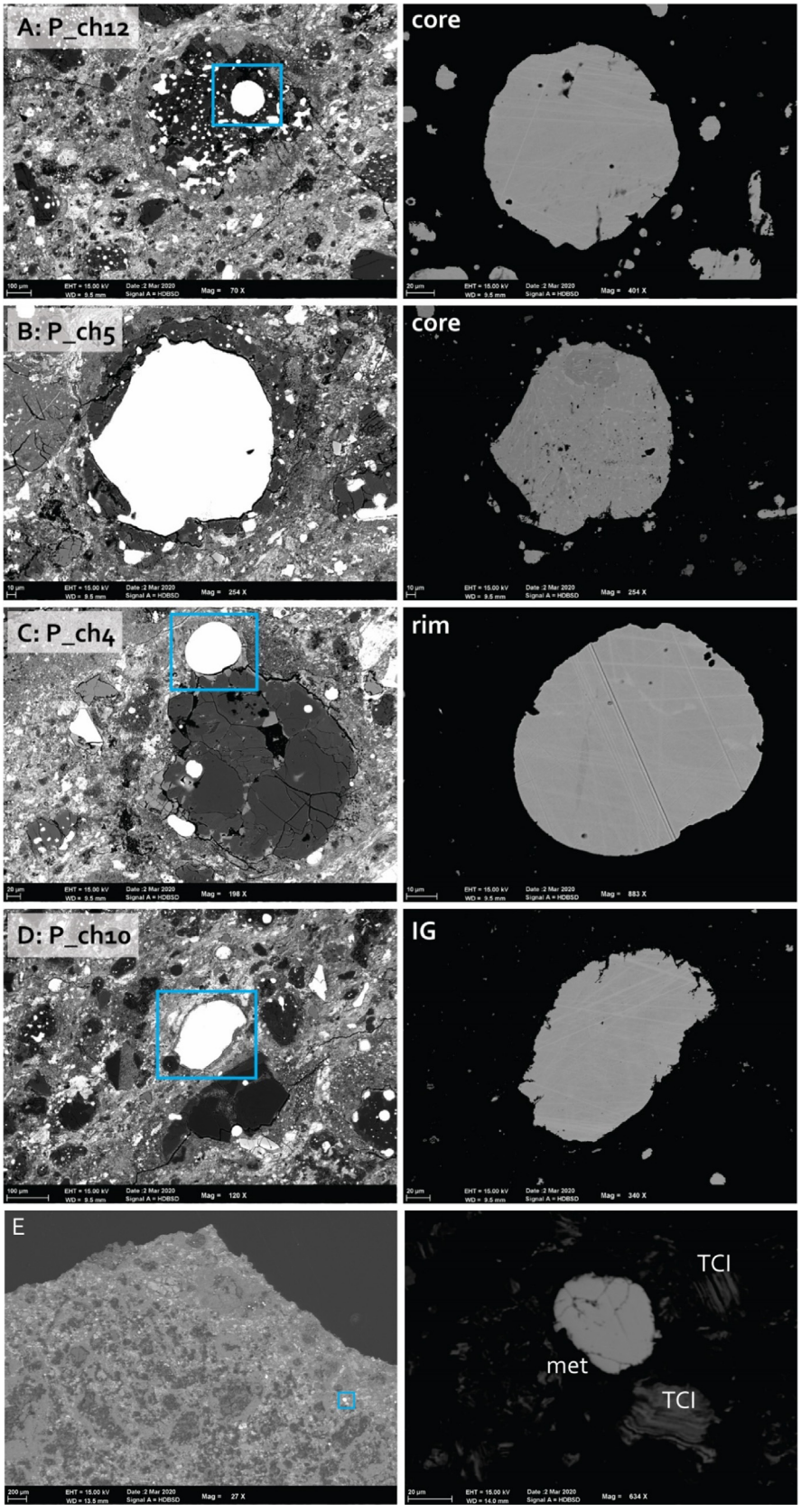
grains from the Leoville C5 chondrule (Fig. 5D, Table 1) lies along the correlation for the CR and CM chondrite metal. Other averaged data from Leoville chondrules are not plotted here but show more scatter away from this correlation. The few sulfides from Leoville chondrule rims measured in this study have low Ni and Co concentrations and plot on the solar line.

3.2.2. Ni content in various petrological settings

The Ni content of chondrite metal in different petrological settings was investigated to further investigate plausible causes for the previously observed contrasts in chondrule core versus rim concentrations and implications for their respective origins (Wasson and Rubin, 2010; Jacquet et al., 2013). We have investigated the Ni content within individual metal grains and between grains of chondrule cores, rims and isolated grains (Fig. 6). For CR chondrite metal, individual grains of the cores and the isolated grains show relatively small inter-grain variations (<0.2 wt.%). The chondrule rims are more heterogeneous (<1.2 wt.% variation). The Ni contents of CR chondrule cores are significantly higher (7.3 ± 0.7 wt.%, 2SD) than the rims (5.4 ± 1.0 wt.%, 2SD) and the isolated grains (5.1 ± 0.2 wt.%, 2SD), in agreement with previous measurements (Wasson and Rubin, 2010; Jacquet et al., 2013). A similar trend occurs for the Paris metal grains (Fig. 6A), although for these grains it was more difficult to establish if grains represented core, rim or isolated settings. Maribo isolated grains have very constant Ni contents (on average 4.9 ± 0.6 wt.%, 2SD), which are indistinguishable from Paris rims and isolated grains (~4.7 wt.%, 2SD). For Bells, the chondrule core Ni contents are similar to rims and isolated metal grains from CR and CM chondrites (4.7 ± 2.0 wt.%). In contrast, Bells' isolated grains have high Ni contents (6–11 wt.%) and appear to have a composition distinct from the chondrule metal. The Ni contents of Leoville metal are highly variable and related to kamacite-taenite exsolutions within the individual grains. Nevertheless, the averaged Ni compositions for Leoville chondrule core metal (5.5 ± 2.1 wt.%, 2SD) overlap with Paris' core compositions and are in agreement with previous analyses of core metal from Leoville (4.8 ± 0.3 wt.%, Zanda et al. 1994). The sulfides analyzed in Leoville are low-Ni troilite grains that co-exist with metal in the rims surrounding the chondrule cores, unlike the troilite that co-exists with low-Ca-pyroxene in the chondrule igneous rims (Marrocchi and Libourel, 2013). The Ni content in these sulfides is mostly below the detection limit. In contrast, the co-existing metal rim grains have higher Ni contents than the core metal (5–10 wt.%), similar to the two isolated metal grains found in the Leoville sections.

3.3. LA-ICPMS analyses of metal grains

The averaged trace element concentrations of CR, CM, CM-an and CV chondrule core, rim and isolated metal grains are reported in Table 2. EMP and LA-ICPMS data is combined and visualized in Figs. 7–10 by plotting CI normalized concentrations with increasing volatility of the elements. All condensation temperatures mentioned in this


A: P_ch12
core
B: P_ch5
core
C: P_ch4
rim
D: P_ch10
IG
E
TCI
met
TCI

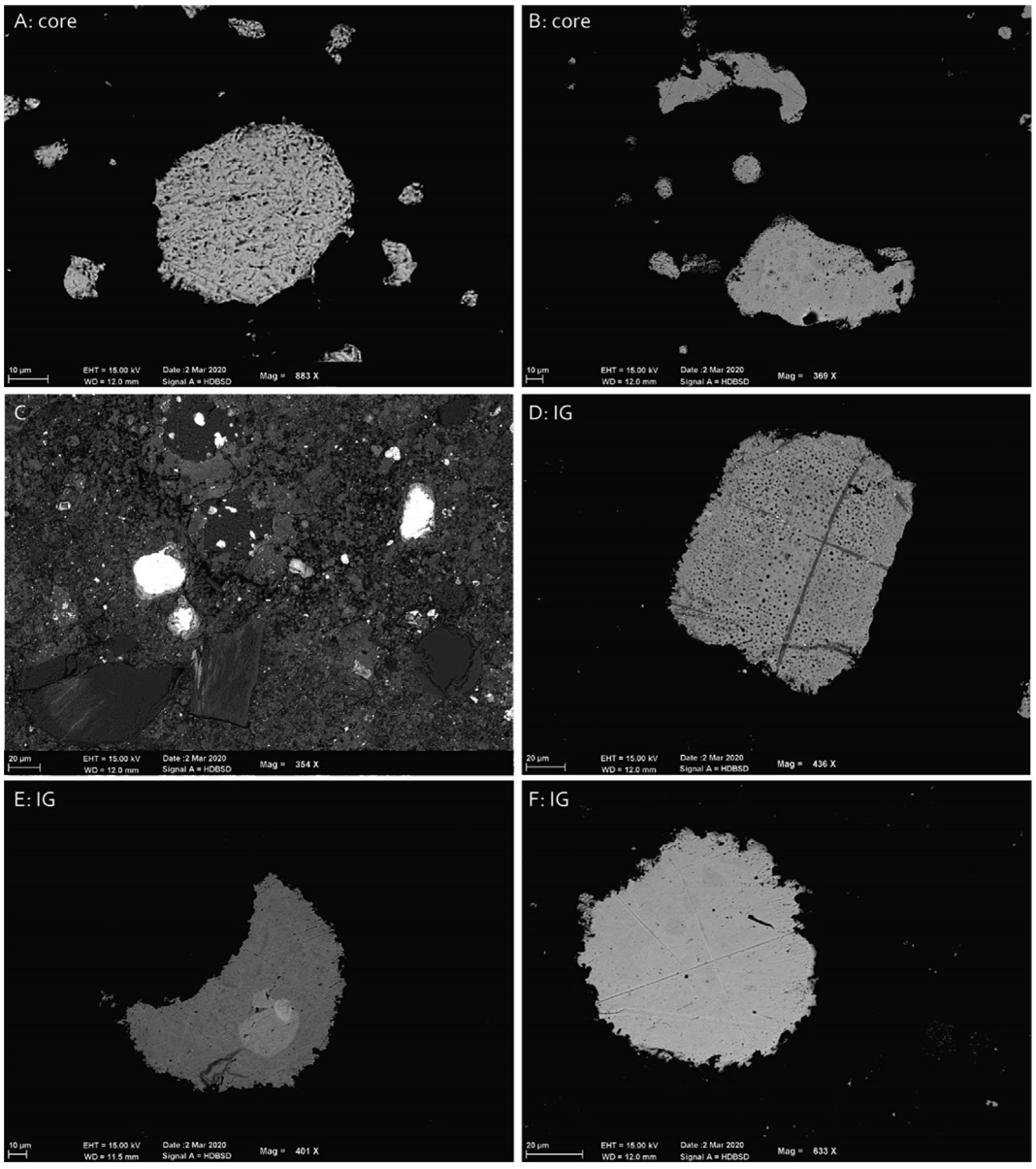


Fig. 3. Back scattered electron images of representative Bells metal grains. A and B are grains from chondrule cores ch1 and ch2, with and without black inclusions. C is an overview of the Bells chondrite section, showing a high-porosity altered matrix with metal-rich chondrules and isolated chondrule grains. D, E and F are isolated grains (IG: met3, met6, met7) within the matrix with irregular boundaries due to oxidation and with or without black inclusions. High resolution BSE images of all Bells metal grains used in this study can be found in Fig. S7.

study are from Lodders (2003). Table S4 in the Appendix provides the LA-ICPMS analyses of individual ablated spots and grains. The Cr concentrations of the metal grains are analyzed by EMP and LA-ICPMS and their values with corresponding 2SD errors are identical. For example, EMP data from NWA801 cores, rims and isolated grains yield 0.29 ± 0.08, 0.37 ± 0.19 and 0.24 ± 0.22 wt.%, respectively (Table 2). LA-ICPMS data shows averages of 0.29 ± 0.08,

Fig. 2. Back scattered electron images of representative Paris CM chondrite metal grains. A and B are grains from chondrule cores. Grain ch5 is the only grain with significant kamacite-taenite exsolution features. C is a metal rim grain and D is a potential isolated grain. Left panels show the petrological settings of the grains and right panels show the high-contrast, low luminosity images of the corresponding grains (zoom-in of left panel blue boxes). High resolution BSE images of all Paris metal grains used in this study can be found in Fig. S6. (E) Overview of Maribo section with a metal grain (met1) within the blue square. (B) Zoom-in of the blue square with high contrast, low-luminosity setting. TCI = tochilinite-cronstedtite intergrowth.

0.35 ± 0.19, 0.22 ± 0.18 wt.%, respectively (Table 2). This gives a good indication of the quality of the LA-ICPMS data as well as the correlation between EMP and LA-ICPMS data (see also Appendix A).

3.3.1. NWA 801 (CR)

The average metal compositions of the CR cores, rims and isolated grains are indistinguishable (Table 2). The 2SD errors of the averaged bulk CR metal concentrations are smaller than the 2SD errors of the averaged core, rim and isolated grains (Table 2). However, looking at the individual volatility patterns of CR metal grains, some important distinctions can be observed. In Fig. 7, we plotted the metal concentrations normalized to CI chondrites versus the 50% condensation temperatures of the elements (Lodders, 2003). We show that the metal grains in the chondrule cores have HSE, W, Mo, Ni, Co and P concentrations that are typically enriched relative to CI chondrites (2–7× CI). The HSE, W and Mo concentrations of the rim metal grains are more variable (Fig. 7b) and some rim grains are depleted relative to CI. The HSE, W and Mo concentrations of the IG within the same range as the core metals and the Ni, Co and Pd concentrations are relatively depleted. In all type locations, Cr has a CI-like concentration, whereas V is more depleted between 0.1 and 1× CI. The more volatile elements, Mn, Cu, Zn and Sn are all depleted relative to CI. Cu, Zn and Sn are most variable between metal grains, but show no systematic dependence on textural setting.

3.3.2. Paris and Maribo (CM)

The distinction between Paris core and rim metal grains is often difficult to make, since most large metal grains are partially surrounded by silicate rims resembling chondrule fragments. Hence, the trace element compositions of the Paris metal core grains shown in Fig. 8 may in part be rim metal grains. However, taking into account only the verified core metal grains shows that the compositional range observed in Fig. 8 a does not change, although it can imply that the composition of the verified rim grains is not representative of all rim grains in Paris. We have analyzed the trace element compositions of three (verified) chondrule rim grains. One chondrule rim (Ch15) contains three < 50 μm grains that are partially surrounded by chondrule silicates and yield similar compositions to the chondrule core metal (Fig. 8a). One of these grains appears more enriched in volatile elements like Mn, Cu and Zn, but also has larger errors on these elements (Table S3 in SI Appendix). Two other chondrule rim grains (Ch4 and Ch13) are 150 and 100 μm in diameter, respectively. These grains are still attached to the host chondrule but are mostly surrounded by matrix material. The compositions of these grains are significantly different from the core metals (Fig. 8b). In detail, all elements with volatilities between Os (T_{50} = 1812 K) and Rh (T_{50} = 1392 K) have abundances that are more depleted than CI chondrites (0.1–0.9× CI). The more volatile elements (T_{50} < 1392 K) have identical concentrations to the metal grains from the Paris chondrule cores. The overall volatility patterns of the Paris isolated grains (C1 and perhaps C8, C10 and C14) are similar to that of the core metals (Fig. 8a). We were able to analyze one isolated grain from Maribo (~30 μm), for which the volatility pattern was distinct from any Paris metal grain (Fig. 8a). The overall pattern is flat compared to the Paris metal grains, with siderophile and chalcophile element concentrations between 1–4× CI. Elements in the Maribo IG with condensation temperatures between that of V and P (1229 K > T_{50} < 1370 K) have similar concentrations to Paris metal grains. Elements with higher T_{50} are depleted compared to Paris and the most volatile elements with lower T_{50} are enriched between 1 and 4× CI.

In Fig. 11d, we have compared the core metal compositions of Paris to those of NWA 801. The latter generally overlap with the Paris core grains, except for V, Cr and Mn, which are more enriched in Paris metals. Other elements, including PGE (except Pd), W, Mo, Cu and Zn, overlap with the low concentration endmembers of Paris metals. Overall, while the HSE, Ni and Co average concentrations of Paris and NWA801 follow each other closely, concentrations of less siderophile elements are more enriched in Paris metals.

3.3.3. Bells (CM-an)

Bells metal grains can be divided into chondrule core metal and isolated metal grains. Chondrule core grains are mainly small (<20 μm) and so we have measured only two core grains by LA-ICPMS. Isolated metal grains are more abundant and larger (50–100 μm) and six were analyzed for trace elements. Except for Pd, the PGE, W and Mo concentrations of Bells core metal are CI-like or slightly depleted relative to CI chondrites (Fig. 9). In contrast, the HSE and Mo concentrations of Bells IG are strongly enriched relative to CI chondrites (>10× CI), whereas W is more depleted (<5× CI). As mentioned before (section 3.3.1), Ni and Co concentrations are also enriched in IG relative to the chondrule cores. Bells IG and core metals show similar depletions in V and Cr relative to CI chondrites. Mn, Zn and Sn concentrations of both metal type localities overlap and show similar depletions relative to CI chondrites as NWA 801 core metal (Fig. 11b). Cu is unusually depleted in Bells IG.

Bells metal grains are compared to Paris and NWA 801 chondrule core metal (Fig. 11a and b). The isolated grains do not match the compositions of CM and CR chondrite metals. The volatility patterns of the Bells core metal most closely resemble that of Paris rim metals (i.e. the larger grains Ch4 and Ch13).

3.3.4. Leoville (CV)

LA-ICPMS analyses of Leoville metals are limited to core and rim grains (Fig. 10). Their compositions largely overlap, except for the HSE that are increased in the rim relative to the core grains. The chondrule core metals of Leoville are compared to those of NWA 801 (Fig. 11c), generally showing the same volatility patterns. However, there are some marked differences between the two chondrite groups: while HSE, Ni and Co concentrations are indistinguishable, W and Mo in Leoville metals have more elevated concentrations and V, Cr, Mn, Cu, Zn and Sn concentrations are significantly higher. In contrast, Leoville metal P

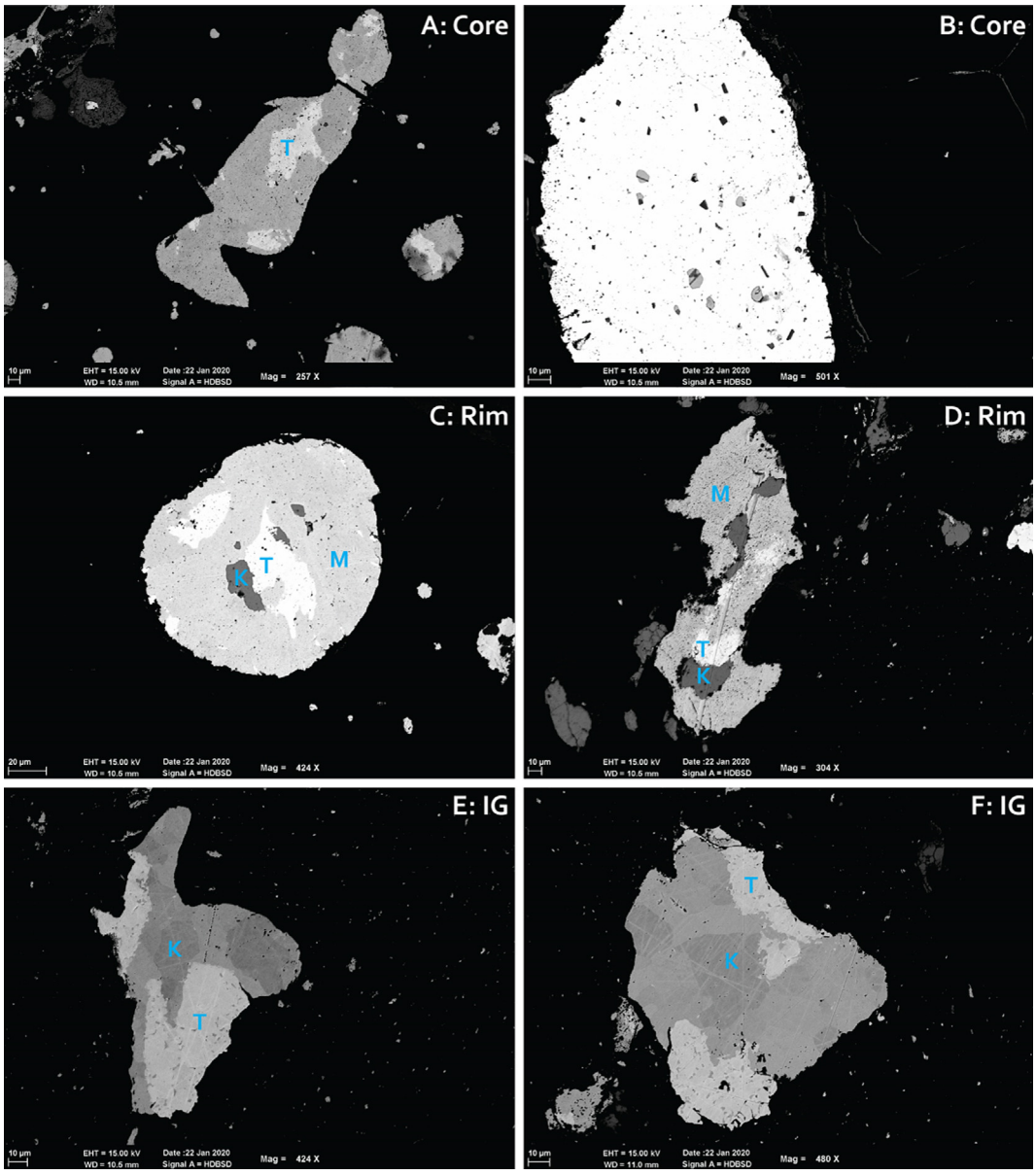


Fig. 4. Back scattered electron images of representative Leoville metal grains. A and B are grains from chondrule cores (ch3 and ch1), with taenite (T) exsolutions, black inclusions and grey silica inclusions in the case of ch1 (panel b). C and D are rim grains (c5 and met1), with kamacite (K) and taenite exsolutions in a martensite (M) host metal. E and F are isolated grains (IG). High resolution BSE images of all Leoville metal grains used in this study can be found in Fig. 8.

concentrations are below EMP detection limits and are, thus, significantly smaller compared to NWA 801 metals.

4. DISCUSSION

4.1. The effect of secondary alteration on metal composition

The significance of chondritic metal compositions is only understood when they can be regarded as primary features, meaning they are unaffected by secondary alteration on chondrite parent bodies, thermal overprinting from impact shocks and/or terrestrial weathering. Hence, we consider in this section the effect of potential secondary effects on the chondrite metal composition.

Firstly, NWA 801 is considered to be an unshocked CR chondrite (Charles et al., 2018) that experienced a limited amount of aqueous alteration (van Kooten et al., 2019) and has not been affected by thermal overprinting (Briani et al., 2013). Nonetheless, this chondrite is characterized by moderate to extensive terrestrial weathering (Schrader et al., 2011), as evidenced by pervasive veins of Fe-rich rust and oxidized rims surrounding metal grains throughout the section. However, the weathering is mostly limited to rim metals and isolated grains in the matrix. While it is clear

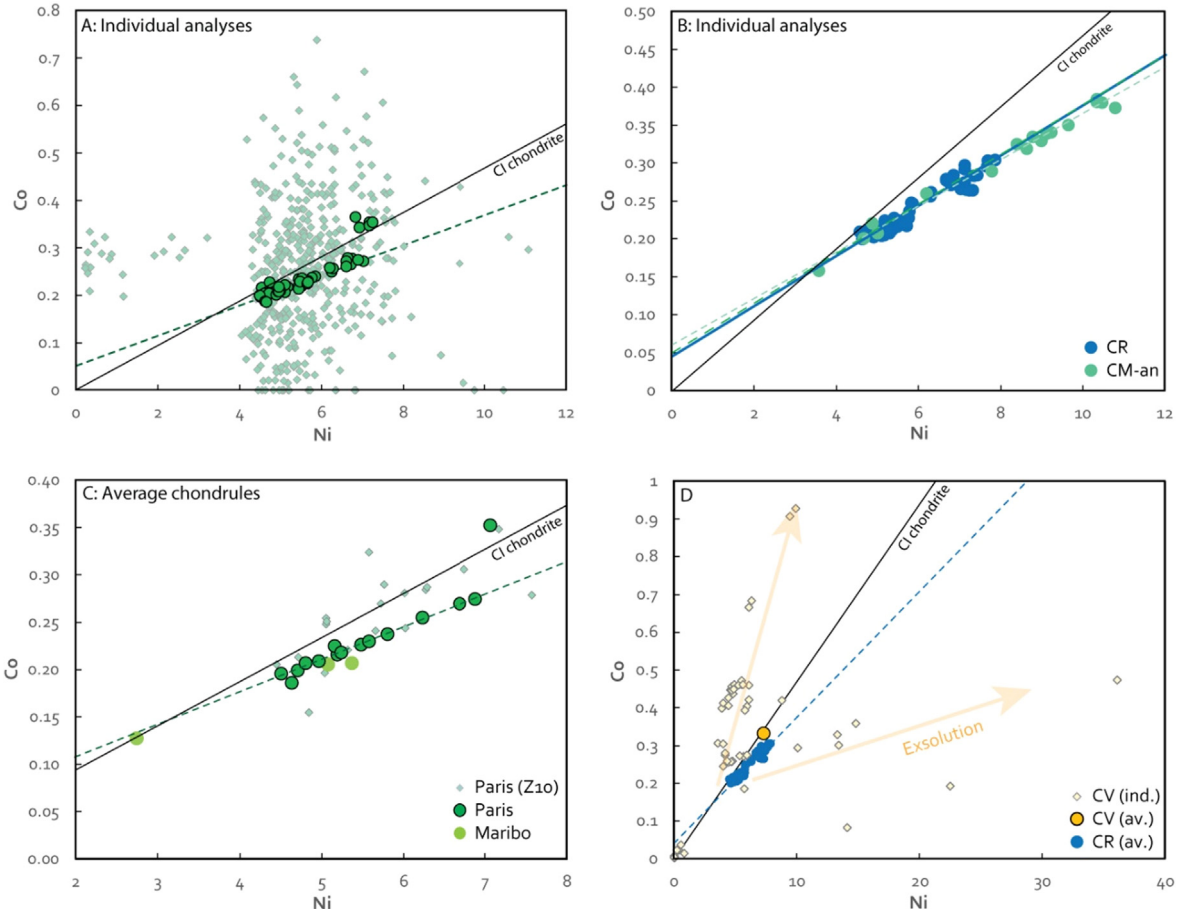


Fig. 5. Plots of Co versus Ni in wt.% from Paris metal EMP data, where (A) shows individual point analyses from Paris metal grains from Hewins et al. (2014) and individual 30 μm raster analyses from this study; (B) Individual raster analyses from CR chondrite NWA801 and CM-an Bells. Trend lines through these data and Paris metal are shown; (C) Averaged data from various chondrules and isolated grains in Paris and Maribo and from Z10 data; (D) Individual data from Leoville metal and sulfide grains, with the CR chondrite metal for reference. Only one averaged chondrule metal composition is shown: for this chondrule (C5) we have both core and rim data from Table S3. Other averaged chondrules are not shown here, but scatter throughout the plot.

that the oxidation of the metal grains has attacked the outer edges of the grains, we tested the potential change in composition through oxidation by setting EMP spot locations from the core to the edge of an isolated metal grain (~1 mm diameter) surrounded by a thick oxidation rim (~100 μm). The spots at the edge of the seemingly unaltered part of the metal grain (Table S4, NWA#23 and #27) showed a negligible and non-systematic variation in Ni, Co, Cr, S and P relative to the core spots (Table S4, NWA#24–26). Consequently, at least for major and minor elements measured by EMP, no observable compositional change in the metal grains is recorded due to terrestrial weathering. The metal chondrule rims from NWA 801 record a higher variability of HSE (Fig. 7a), which may be attributed to mobility of these elements by leaching during terrestrial weathering. However, the HSE volatility patterns of rim metals behave the same as those of the core metals (Fig. 13e), suggesting that secondary alteration is not responsible for this higher variability, in agreement with a recent assessment of weathering effects on HSE in NWA 801 (Nakanishi et al., 2021). Moreover, terrestrial weather-

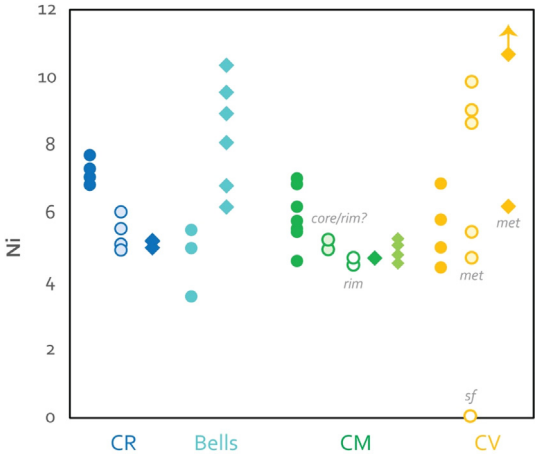


Fig. 6. Ni of core (solid spheres), rim (open spheres) and isolated metal (diamonds) from CR, Bells, CM (light green for Maribo) and CV chondrites.

Table 2
LA-ICPMS data in ppm from core, rim and isolated metal grains in NWA 801, Leoville, Paris and Bells. All errors are given as 2SD, which reflects the standard deviation from the mean calculated from all core, rim or IG analyses in Table 1. N is the number of analyses done, excluding rejected data (see text for explanation).

	NWA 801 (CR)							**Leoville (CV)**			
	core	2SD	**rim**	2SD	**IG**	2SD		**core**	2SD	**rim**	2SD
n	*10*		*20*		*14*		***n***	*7*		*8*	
V	17.3	7.2	13.2	5.5	11.8	8.1	**V**	107	93	89	42
Cr	2865	834	3538	1932	2213	1852	**Cr**	9486	2121	11,541	16,661
Mn	14.6	18.8	23.7	22.3	21.8	6.8	**Mn**	217	498	76	96
Cu	21.7	40.6	23.5	43.6	28.8	36.2	**Cu**	190	279	367	1144
Zn	0.31	0.58	0.36	0.29	0.30	0.29	**Zn**	22	34	17	34
Mo	3.58	0.82	2.75	3.95	3.40	1.35	**Mo**	5.5	4.3	6.3	2.8
Ru	3.10	0.64	2.86	4.10	3.14	0.98	**Ru**	3.8	1.2	11.4	13.1
Rh	0.38	0.10	0.34	0.48	0.36	0.12	**Rh**	0.46	0.14	1.45	1.34
Pd	3.66	1.18	25.87	94.32	2.73	1.56	**Pd**	3.9	5.0	5.5	12.7
Sn	0.16	0.38	*0.01*	*0.48*	*0.07*	*0.50*	**Sn**	0.65	1.19	1.21	2.76
W	0.34	0.13	0.33	0.50	0.41	0.24	**W**	0.50	0.51	1.13	1.39
Os	2.67	0.75	3.23	4.95	2.80	1.31	**Os**	3.2	1.5	10.8	14.9
Ir	2.38	0.82	2.52	3.95	2.32	0.99	**Ir**	2.6	0.9	8.4	10.7
Pt	3.21	0.65	2.77	4.12	2.98	1.08	**Pt**	3.6	1.3	12.9	20.4
Au	0.33	0.14	0.17	0.18	0.26	0.11	**Au**	0.09	0.07	0.84	1.59

	Paris (CM)							**Bells (CM-an)**			
	core	2SD	**rim**	2SD	**IG**	2SD		**core**	2SD	**IG**	2SD
n	*29*		*2*		*1*		***n***	*2*		*6*	
V	52.1	76.9	77.0	121.6	66.0	18.0	**V**	3.36	0.47	3.62	2.59
Cr	5533	3368	8260	2121	13,200	3600	**Cr**	1337	218	1874	1003
Mn	50	105	594.5	468.1	174.0	76.0	**Mn**	30	6	11	28
Cu	32.9	70.0	100.6	63.5	102.0	26.0	**Cu**	217.5	196.6	0.7	0.9
Zn	0.85	4.83	42.70	97.02	3.00	2.20	**Zn**	0.28	0.14	0.53	1.29
Mo	4.25	4.18	1.97	3.65	3.47	0.93	**Mo**	0.62	0.05	7.10	3.39
Ru	3.99	4.08	1.85	3.15	2.97	0.51	**Ru**	0.70	0.03	10.76	4.78
Rh	0.53	0.60	0.23	0.47	0.21	0.04	**Rh**	0.08	0.04	1.29	0.60
Pd	2.96	1.38	2.68	0.27	4.60	1.20	**Pd**	2.19	0.44	4.04	1.37
Sn	0.15	0.21	0.58	1.20	0.60	0.27	**Sn**	0.30	0.18	0.17	0.15
W	0.42	0.44	0.34	0.68	0.48	0.17	**W**	0.09	0.03	0.16	0.08
Os	3.27	3.62	1.70	3.05	3.65	0.66	**Os**	0.92	0.63	9.50	2.99
Ir	2.95	3.25	1.47	2.86	3.54	0.59	**Ir**	0.75	0.48	9.15	2.53
Pt	4.34	4.86	1.89	3.38	2.00	0.29	**Pt**	0.58	0.21	10.42	3.86
Au	0.24	0.28	0.31	0.00	0.25	0.06	**Au**	1.43	1.33	1.87	2.70

ing and oxidation of mineral phases is characterized by Re depletion and Os uptake, whereas it does not seem to affect the other HSE (Hyde et al., 2014). While Re was not quantified in our data, an Os uptake in the metal rims relative to the cores was not observed.

The CM chondrites Paris and Maribo are among the least altered samples from their group (Bourot-Denism et al., 2010; Haack et al., 2012; Hewins et al., 2014; van Kooten et al., 2018), with Maribo being more affected by aqueous alteration and terrestrial weathering than Paris. The latter consists of areas that are more and less altered (Hewins et al., 2014). In the least altered metal-rich areas we analyzed the metal grains, of which some are altered and oxidized at the grain boundaries (Fig. 2d). This is likely the result of limited aqueous alteration rather than terrestrial weathering. The freshness of the fusion crust of Paris and its Na/K ratio suggest that this meteorite was collected before any significant terrestrial modifications occurred (Hewins et al., 2014). Similar to NWA 801, the very limited variation of major and minor element concentrations within metal grains suggests that leaching of siderophile elements during aqueous alteration was negligible. Likewise, the small metal grains of Maribo show scant signs of secondary alteration. Terrestrial weathering of Maribo was more extensive than Paris, because Maribo was collected after a month of rain in Denmark (Haack et al., 2012). However, this weathering was likely limited to the enrichment of highly mobile elements (U, Sr, Ba, Rb, and Cs; (van Kooten et al., 2019)) and depletion of Na (Haack et al., 2012) in the bulk rock. Collectively, these results suggest that the metal compositions of Paris and Maribo are primary features.

Bells is the most altered carbonaceous chondrite investigated. It shows pervasive aqueous alteration of chondrules and matrix and a significant fraction of initial metal was converted to magnetite (Mittlefehldt, 2002; van Kooten

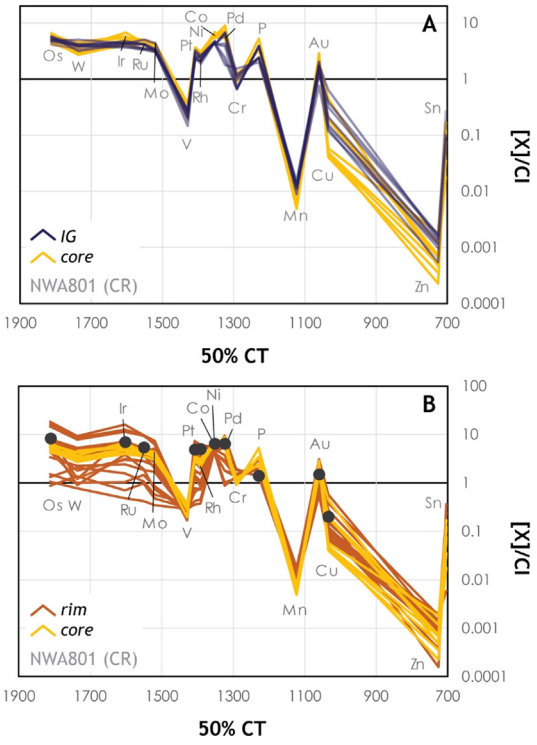


Fig. 7. Concentrations normalized to CI chondrites in CR chondrite metal grains from NWA 801 plotted against the 50% condensation temperature of siderophile and chalcophile elements (Lodders, 2003). (A) Core metal grains versus isolated grains (IG) and (B) core metal grains versus rim grains. Black dots are averaged core compositions from Jacquet et al. (2013). Each line corresponds to a single grain. The data encompasses grains from 3 chondrule cores, 4 chondrule rims (of which one chondrule-rim pair ch1, see Appendix Table S4) and 3 isolated grains.

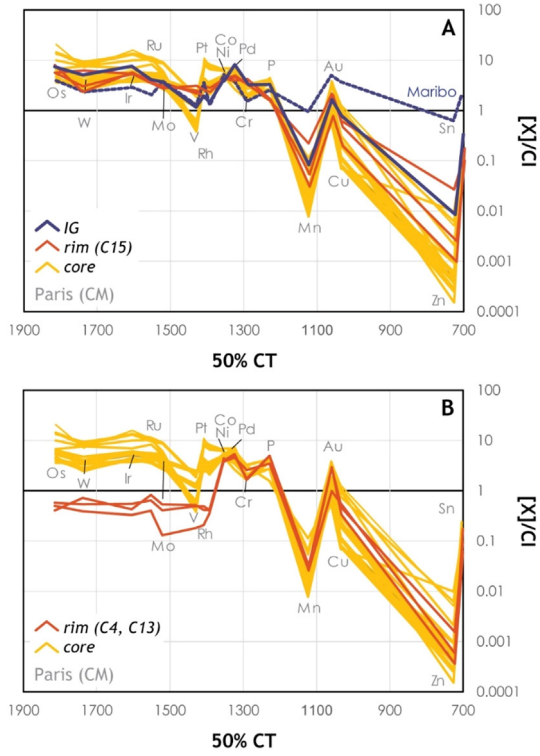


Fig. 8. Concentrations normalized to CI chondrites in CM chondrite metal grains from Paris and Maribo plotted against the 50% condensation temperature of siderophile and chalcophile elements (Lodders, 2003). (A) Core ($n = 24$), rim (C15, $n = 3$) and isolated metal grains ($n = 2$). Each line corresponds to a single grain. The data encompasses grains from 13 chondrule cores, 1 chondrule rim and 1 isolated grain. (B) Core and rim (C4, C13; $n = 3$) compositions from Paris.

et al., 2018). Even so, Bells retains a significant portion of relatively unoxidized metal grains that are characterized by similar Co/Ni ratios as CR and CM chondrite metal (Fig. 5c). Most of these grains are isolated and are surrounded by an oxidized phase, whereas the unoxidized metal cores – although showing various exsolved phases between the metal grains (Fig. 3) – have relatively constant volatility patterns (Fig. 9). Similar to CR and CM metals, Bells' metal composition shows limited inter-grain variability. We thus propose that the Bells metal grains experienced a negligible effect from secondary alteration.

The Leoville CV chondrite has experienced moderate terrestrial weathering (Abreu and Brearley, 2005) as well as a low degree of thermal metamorphism (Bonal et al., 2016). The latter has resulted in exsolution of martensite into kamacite and taenite (Fig. 4). Moreover, the low concentrations of P in CV relative to CR chondrules is likely the result of schreibersite oxidation during thermal metamorphism. Along with these exsolved metals, sulfide grains are sometimes found surrounding or interspersing the metals in chondrule cores (Fig. 12a), the rims (Fig. 12b) and isolated grains (Fig. 12c). These sulfides are typically fine-grained (<50 μm), irregularly shaped, and do not show any exsolution features that could define them as high-temperature pre-accretionary objects (Visser et al., 2019). In more metamorphosed CV chondrites such as Allende, sulfides are more abundant within the chondrules, suggesting mobilization of S during secondary alteration (van

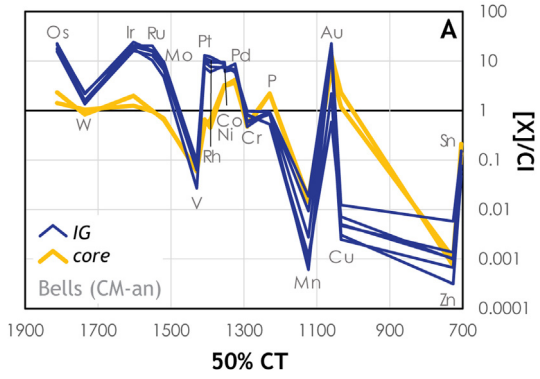


Fig. 9. Concentrations normalized to CI chondrites in CM-an chondrite metal grains from Bells plotted against the 50% condensation temperature of siderophile and chalcophile elements (Lodders, 2003). Core ($n = 2$) and isolated metal grains ($n = 6$). Each line corresponds to a single grain. The data encompasses grains from 2 chondrule cores and 6 isolated grains.

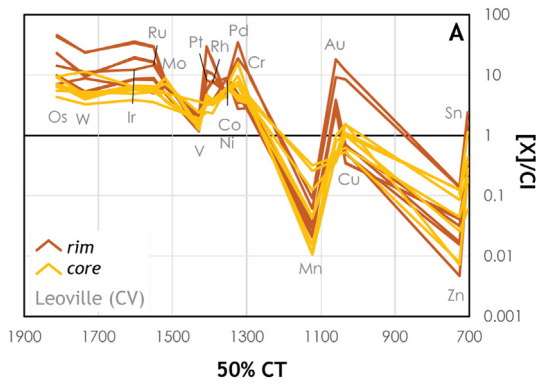


Fig. 10. Concentrations normalized to CI chondrites in CV chondrite metal grains from Leoville plotted against the 50% condensation temperature of siderophile and chalcophile elements (Lodders, 2003). (A) Core ($n = 7$) and rim metal grains ($n = 8$). Each line corresponds to a single grain. The data encompasses grains from 2 chondrule cores and 3 rim grains.

Kooten and Moynier, 2019). The sulfides consist of relatively pure FeS, with minor elements such as Cr, P, Ni, Co and Cu below the detection limits of EMP analyses (Table 1). The metals associated with these secondary sulfides were avoided during LA-ICPMS analyses. Furthermore, we suggest that the LA-ICPMS analyses of Leoville metal grains (three spots with diameter of 40 μm for each grain and kamacite/taenite phases typically <20 μm) reflect the bulk metal, rather than the exsolved phases. Indeed, the Cr concentration obtained by averaging the EMP analyses of taenite and kamacite within single grains (Table S3) matches the LA-ICPMS values (Table S4).

4.2. Implications of a subsolar Co/Ni ratio in chondritic metal grains

Previous analyses of carbonaceous chondrite metal grains have shown that the Co/Ni ratio is solar or CI-like (Connolly et al., 2001; Krot et al., 2002; Wasson and Rubin, 2010; Jacquet et al., 2013; Hewins et al., 2014), although it has been remarked that metal grains with high Ni concentrations have a tendency for subsolar Co/Ni ratios (Wasson and Rubin, 2010; Jacquet et al., 2013). Solar Co/Ni ratios have been interpreted as a condensation origin for chondrule metals, since Ni and Co have similar condensation temperatures (Lodders, 2003). However, this has been at odds with the positive correlation found between

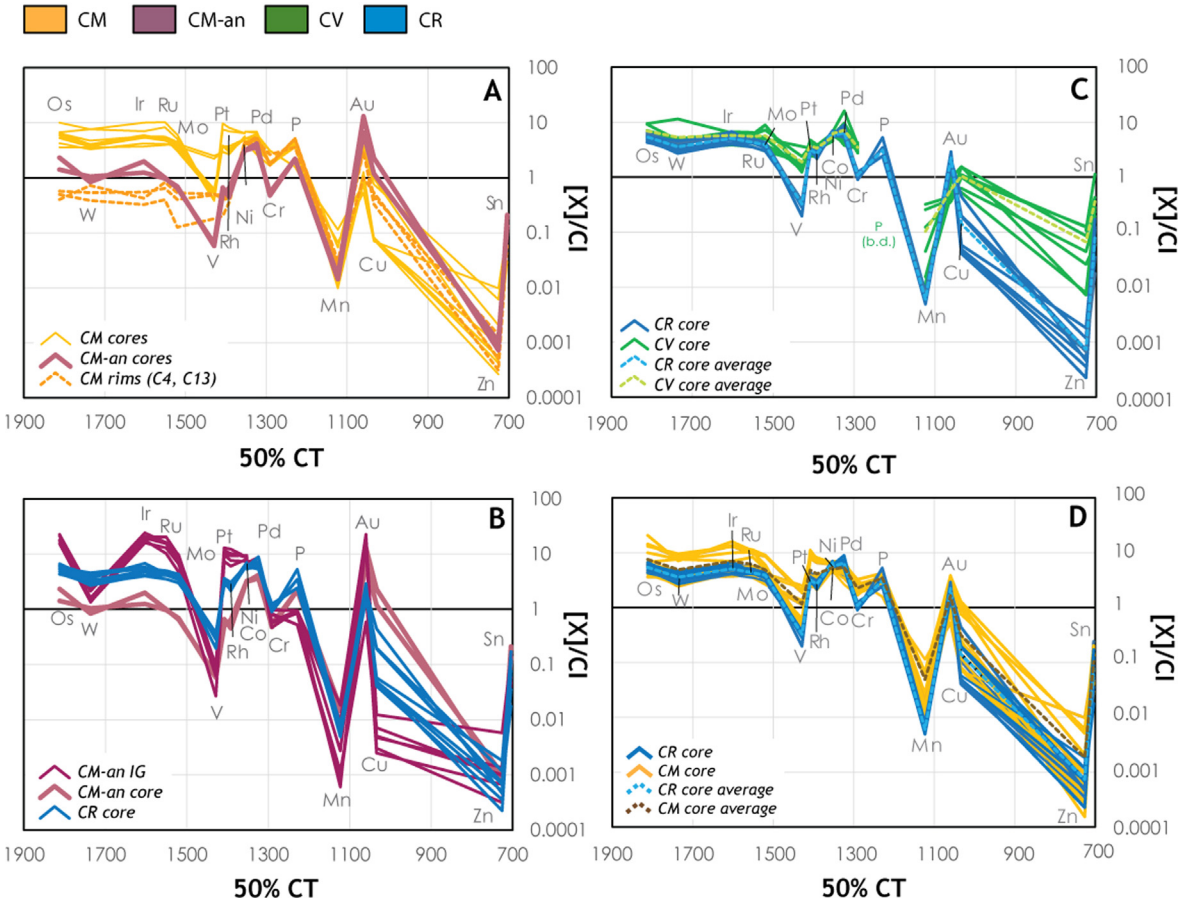


Fig. 11. Concentrations normalized to CI chondrites in CM, CM-an, CV and CR chondrite metal grains plotted against the 50% condensation temperature of siderophile and chalcophile elements (Lodders, 2003). (A) Compositions from CM core metal, CM rim metal (C4, C13) and CM-an core metal. (B) Bells IG and core metal grains versus NWA 801 core metal grains. (C) Leoville versus NWA801 core metal grains and their averages. (D) Paris versus NWA 801 core metal grains and their averaged compositions.

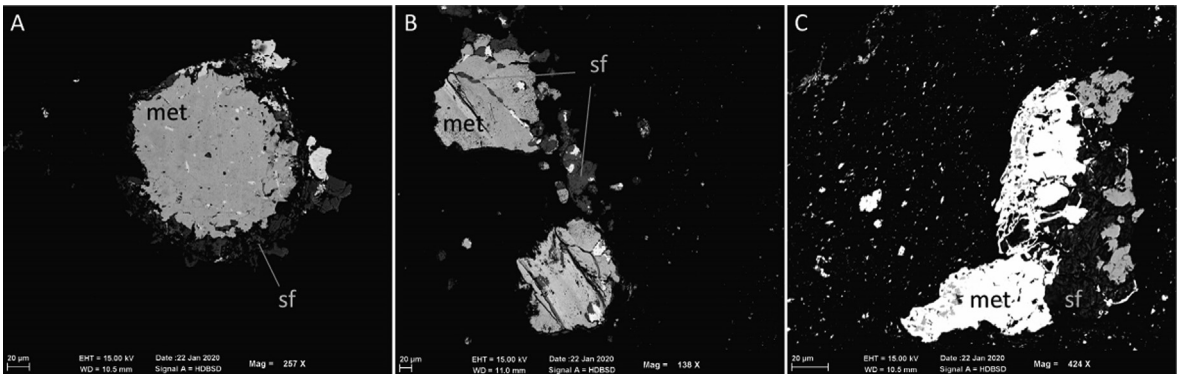


Fig. 12. Metal grains from Leoville that show secondary alteration features of metal being modified to sulfide. (A) Chondrule C5 core grain with sulfide rim, (B) Chondrule Ch4 rim grains intersected by sulfide veins and (C) Isolated metal grain (not analyzed in this study) partially altered to micron sized sulfide grains.

the partition coefficient of Cr between metal and olivine and the Fe content of olivine (Zanda et al., 1994; Jacquet et al., 2013), which favor metal-silicate equilibration. Here, we show that using a different analytical approach to measuring the Ni and Co contents (see Section 3.2.1), all metal grains from carbonaceous chondrites (except Ch5 in Paris) fall on a subsolar Co/Ni correlation (Fig. 5).

Previous analyses of CH chondrite metal grains and accompanying models of equilibrium fractional condensation have shown that a subsolar Co/Ni ratio can also be expected during condensation, assuming Ni condenses ahead of Co (Meibom et al., 1999; Campbell et al., 2001; Campbell and Humayun, 2004). This condensation curve (Fig. 14a, dashed grey line) is among others dependent on the activity coefficient γ of Ni and Co in the metal phase (Campbell et al., 2001). The values of γ_{Ni} and γ_{Co} used to calculate the condensation curve in Fig. 14a are 0.65 and 1.05, respectively (Hultgren et al., 1973). More recently, Wood et al. (2019) has reappraised the 50% condensation temperatures of the elements and used the Miedema model to calculate γ from the thermodynamic relationship (Boom et al., 1983), thus obtaining non-ideal mixing behaviors notably for Co with $\gamma_{Ni} = 0.68$ and $\gamma_{Co} = 0.85$. The lower value of γ_{Co} would result in a condensation curve lying closer to the solar Co/Ni ratio within the calculations from Campbell et al. (2001). Condensation calculations of Ni and Co by Grossman and Olsen (1974) model Co as condensing ahead of Ni if both elements are treated as ideal solutions. The uncertainties that these activity coefficients provide to the condensation models of metals are not taken into account in the condensation curve of Fig. 14a, but the reader should be aware of them, since at face value, our data and accompanying errors fall below the curve. Hence, most CR, CM and CM-an metal grains do not seem to reflect a condensation origin and/or were modified after condensation. In agreement with this proposition, vanadium has a very low γ and is supposed to dissolve rapidly in Fe alloys together with Pd during condensation (Wood et al., 2019). However, the V content relative to CI chondrites is low (0.1–1× CI), also compared to the relative Pd content (1–10× CI).

In Fig. 14b, we have plotted Ni versus Cr concentrations of CR, CV, CM and CM-an metal grains together with equilibrium condensation models (solid curve: Grossman and Olsen, 1974; right dashed line: Meibom et al., 1999) and condensation models with complete isolation of gas and solid phases during condensation (left dashed line: Meibom et al., 1999). The overall pattern combining all chondrite groups resembles the curvature of the condensation lines, but most data plot below the equilibrium condensation line. The notable exception is again Paris Ch5, together with some other metal grains from Paris (Ch12 and Ch14 on the line, and lying closely left of the curve: Ch3, Ch7 and Ch9), which can all be classified as core metal grains, roughly 100 μm in diameter. All Paris, Bells and Leoville (single averaged chondrule, see Figs. 5 and 14 caption) chondrule metal grains fall within the Ni versus Cr space defined by the condensation curves from Meibom et al. (1999). This observation suggests that CM (and perhaps CV) chondrule metals are products of equilibrium condensation from a solar gas or from condensation with partial to complete isolation from the gas phase. Note that isolated metal grains from Maribo plot below these condensation curves (Fig. 14b).

In contrast, metal grains from NWA 801 and isolated metal grains from Bells typically fall below these curves, suggesting an alternative origin for these grains. One solution may be metal-silicate equilibration during chondrule formation (Zanda et al., 1994), during which Ni behaves more siderophile than Co (Righter, 2003).

What is particularly interesting about this subsolar Co/Ni correlation, is that all metal grains in different petrological settings and chondrite groups fall on the same correlation line. Assuming an interpretation of metal-silicate equilibration is correct, this suggests that Co and Ni behaved similarly during metal-silicate equilibration of chondrule formation. For every chondrule silicate-metal pair that formed, Ni always becomes more siderophile than Co to the same degree. This would allow for different P-T-fO_2 conditions of chondrule formation, if the partition coefficients of Ni and Co would behave identical during changes the chondrule forming environment. This may be

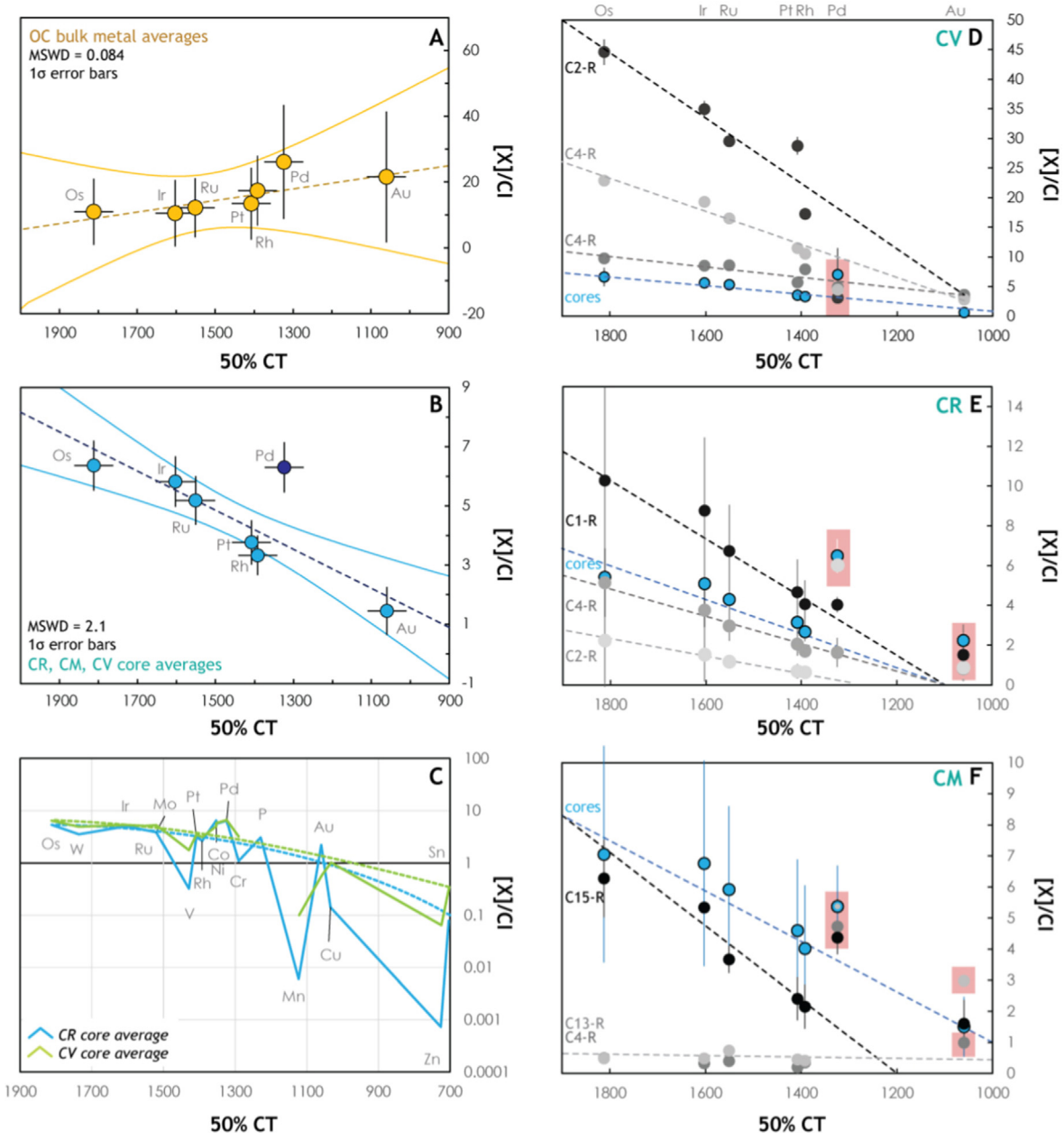


Fig. 13. Volatility patterns of HSE: HSE concentrations normalized to CI chondrites versus 50% condensation temperatures. Note the linear y-axis scale in panels A, B, D–F. (A) Ordinary chondrite (OC) bulk metal compositions from (Okabayashi et al., 2019). A Yorkfit regression is used, plotted with error envelope. The errors shown are 1SD of the mean. (B) Same figure as A, but with CV, CR and CM chondrite metal grains from chondrule cores averages in this study. The regression is taken through all HSE, but Pd is rejected as an outlier. (C) Metal grain volatility patterns from averaged CV and CR chondrule cores (solid lines) plotted with CV and CR chondrule core regression lines from panels D and E (dashed lines). (D–F) HSE from CV, CR and CM chondrule core (blue) and rim metal (grey tones). Errors are 1SD. CV rim metals correspond to single grains, whereas CR and CM contain rim averages of multiple grains. Dashed lines are regressions through the most refractory HSE: Os, Ir, Ru, Pt and Rh. The red boxes denote where Pd and Au deviate from these regressions.

true for changes in oxygen fugacity, silicate and metal phase composition, as well as changes in temperature for the high-pressure regime (Holzheid and Palme, 1996; Li and Agee, 1996; Righter, 2003). However, the metal-silicate partition coefficient of Ni increases significantly towards lower pressures, whereas that of Co remains relatively constant (Li and Agee, 1996; Righter, 2003). Moreover, at low pressure ranges up to 2.5 GPa, the temperature dependence of Ni and Co partition coefficients also changes drastically relative to high-pressure regimes (Kegler et al., 2008). Hence, at the relatively low pressures assumed for chondrule formation in a nebular context (i.e., in a gaseous

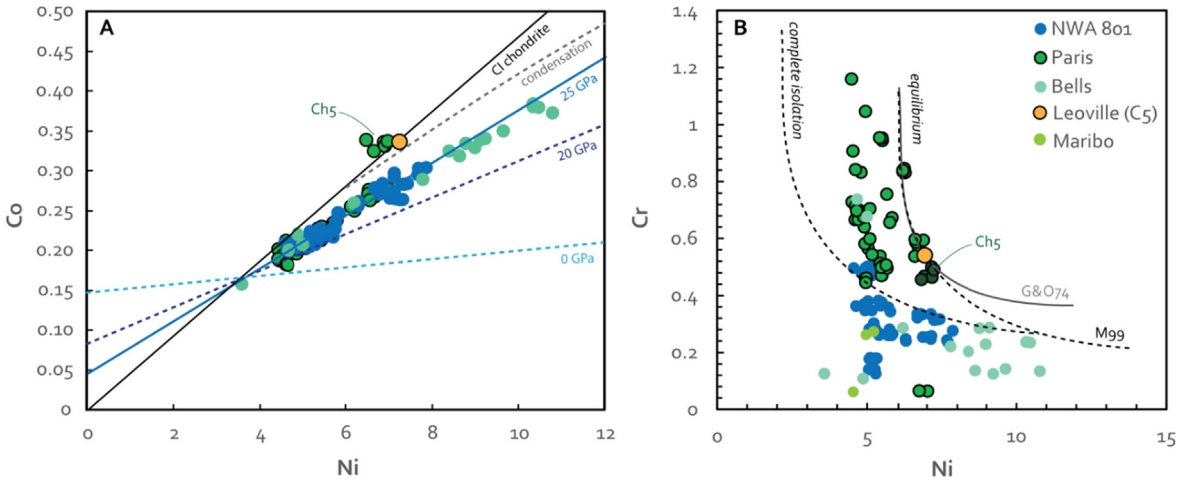


Fig. 14. (A) Ni versus Co (wt.%) of NWA 801, Paris, Bells, Maribo and Leoville metal grains from all petrological settings with a linear correlation plotted through all datapoints except Ch5 from Paris and C5 from Leoville. Also plotted is the CI chondrite correlation (i.e., the solar ratio), the equilibrium condensation curve in dashed grey (Meibom et al., 1999; Campbell and Humayun, 2004) and expected trends for metals that underwent metal-silicate equilibration at 0 GPa and 20 GPa, using partition coefficients from Li and Agee (1996). Note that our data matches best with equilibration around 25 GPa. (B) Ni versus Cr (wt.%) in the same metal grains as panel A. Solid grey curve depicts equilibrium condensation model from Grossman and Olsen (1974), whereas the dashed lines are equilibrium (right) and complete isolation during condensation models (Meibom et al., 1999). The yellow point reflects the averaged composition of core and rim metal grains in chondrule C5 from Leoville (see also Fig. 5).

environment), we would expect variations in P-T conditions to affect the Co/Ni ratio. From the pressure dependence of Ni and Co partition coefficients (Li and Agee, 1996), we have plotted the expected Ni versus Co trends at 0, 20 and 25 GPa (Fig. 14b). We calculate that at high pressures of approximately 25 GPa, we can match the observed Ni versus Co trend of chondritic metal grains. If correct, this implies that CR-like chondrules, or at least their metals, are the by-product of planetary processes, such as impact splashing or jetting (Asphaug et al., 2011; Johnson et al., 2015), meaning their precursor materials could have equilibrated at higher pressures in the mantles of planet(esimals) (equivalent to ~700 km depth). In such a pressure regime, the Co/Ni ratio would not change significantly for a given planet(esimal). However, there have been various valid arguments against such a chondrule formation model, particularly concerning the presence of relict grains (Nagashima et al., 2015; Marrocchi et al., 2018) and the elemental fractionation trends of chondrules (Lichtenberg et al., 2018; Jacquet, 2021). Some of these concerns may be alleviated by invoking the presence of 'dirty' refractory grains in the impact melt plume (Sanders and Scott, 2018). In fact, the silicate phase of a chondrule may not be derived from planetary processes, but could have a nebular origin. From this perspective, it would be relevant to further test the complementary relationship between silicate and metal phases in (individual) chondrules (Zanda et al., 1994; Jacquet et al., 2013). We note that while CM metal grains can be interpreted as having a condensation origin (Fig. 14b), they also plot together with CR metal grains and isolated metal grains from Bells in Ni versus Co space (Fig. 14a). Hence, we cannot rule out a planetary origin for CM metal grains at this point.

4.3. The relationship between core and rim metal grains in chondrules

An important consideration in discussing the origin of chondrules through their bulk compositions is whether the metal rims are produced and chemically adapted in a gaseous medium during the chondrule forming event or if they were later accreted onto the chondrules (Wasson and Rubin, 2010; Jacquet et al., 2013; Jacquet, 2021). We discuss here the compositions of chondrule rim grains relative to the chondrule cores and the implications for chondrule rim metal formation. Relevant observations to this discussion are: (1) larger metal rim grains from CR and CM chondrules show larger offsets from the average core metal HSE composition (Fig. 13e–f). For example, C1-R grains (Fig. 13e) are significantly larger (>200 μm) than the other CR rim grains (<100 μm). Note that the rim metal grains of CV chondrules have highly increased HSE concentrations relative to the core metal grains (Fig. 13d). In these rims, the Co/Ni ratio is also lower than the typical carbonaceous chondrite metal ratio (Fig. 7), suggesting that the elevated HSE in these rim metals are the result of taenite-kamacite exsolution during thermal metamorphism (Okabayashi et al. 2019). This secondary alteration affected W as well (e.g., enrichment of W in the taenite phase), but seemingly had a negligible effect on other elements analyzed here. The Co/Ni ratios of the CR chondrule core metals are not significantly different from those of the rims, although the absolute concentrations are higher. The absolute Ni and Co concentrations of the larger rim metal grains (C1-R) are higher (Ni = 6 wt.%) than the smaller rim grains (Ni = 5 wt.%). (2) Between individual rim grains of an individual chondrule, a large variability in HSE concentrations

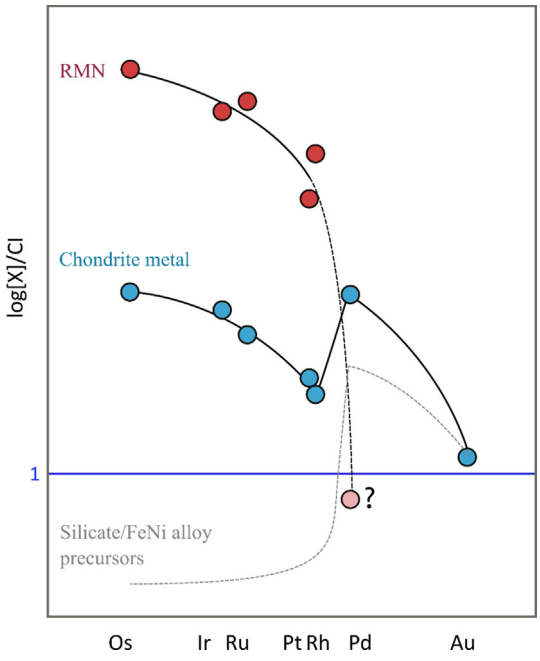


Fig. 15. A sketch of HSE concentrations normalized to CI chondrites of chondritic metal and potential precursors lined up according to their volatility. In red: RMN = the average composition of refractory metal nuggets in carbonaceous chondrites (Daly et al., 2017). The Pd concentration is estimated from RMN condensation models (Campbell et al., 2003); in blue: the averaged chondrite core metal composition from Fig. 13b; grey dashed line: estimated pattern of FeNi alloy and silicate chondrule precursors with 50% condensation temperatures <1350 K.

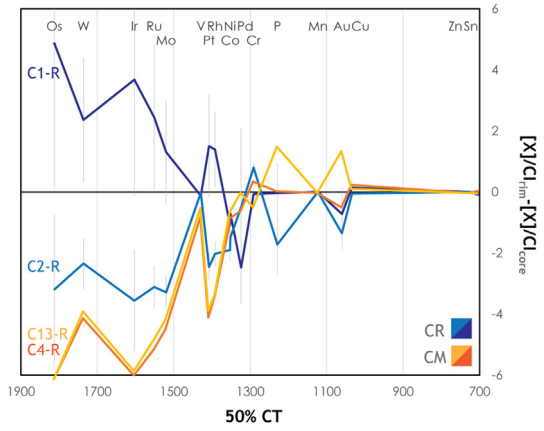


Fig. 16. Volatility patterns of rim metal grains from CR and CM chondrules, with the [X]/CI relative to the average core compositions plotted against 50% condensation temperature of elements. Zero on the y-axis represents the chondrule core metal composition. The rim labels correspond to those in Fig. 13e and f.

exists that is larger the more refractory the HSE. For example, Os has the highest standard deviation when taking the mean rim metal composition of a single chondrule and Au the lowest. (3) Only the most refractory HSE, W, Mo deviate significantly from the core metal compositions (Fig. 16). As mentioned before, Ni and Co are also, to a lesser degree depleted relative to the chondrule core metal. The deviations in siderophile element concentrations of the rim relative to the core metals cannot be explained through evaporation or condensation between an initial core metal composition and a surrounding gas phase (Connolly et al., 2001), since the most volatile elements (e.g., Zn, Sn, Cu, Mn) show no offset from the core compositions and the overall volatility pattern is not consistent with these processes (Fig. 16). The model of Jacquet (2021) applied to the rim metal, where further volatile loss would be prevented by buffering in a gaseous medium, would be applicable, if not for the relative enrichments and depletions in refractory elements alone. A more likely scenario is that these CR rim metal grains - initially identical to the core metal and expelled during chondrule formation – mixed with accreted with refractory metal nuggets (RMNs), rich in HSE and Fe-Ni-Co-poor. During chondrule formation, especially at high temperatures (>2000 K), these micron-sized RMNs would evaporate and recondense on wetted metal surfaces of chondrules or on expelled metal grains. The heterogeneous composition of chondrule metal rims could be attributed to the accretion of metal grains expelled from a multitude of chondrules. The rapid cooling of the chondrule rims then prevented complete homogenization of the final rim metals or recondensation and mixing of elements with lower condensation temperatures.

In contrast, rim metal grains from Paris (e.g. Ch4 and Ch13, Fig. 8b) are depleted in HSE relative to their cores and likely mixed with FeNi alloys. This explains the heterogeneity in composition between individual rim metal grains, as well as the increased variability of more refractory HSE within a single grain.

4.4. The processes that define HSE patterns in chondritic metals

Highly siderophile element patterns in metal grains are used to determine their origin and processes that formed them. Highly siderophile element signatures in chondrule metal are established by (1) mixing of various HSE components during accretion of chondrule precursors in the protoplanetary disk (Grossman and Wasson, 1985; Campbell and Humayun, 2003), (2) FeO reduction and chemical equilibration through metal-silicate partitioning during chondrule formation (Kong and Ebihara, 1997) and (3) evaporation/condensation processes during chondrule formation (Connolly et al., 2001). Under solar nebular conditions, Re, Os, Ir, Ru, Rh, and Pt condense as refractory-metal alloys. Palladium and Au have lower condensation temperatures and condense in solid solution with FeNi metal (Palme 2008). Hence, mixing of refractory metal and FeNi alloys is suggested to, at least partially, explain HSE compositions of metals in CR chondrites (Jacquet et al., 2013).

The HSE patterns of CV, CR and CM chondrite core metals are very similar to each other and all show a general depletion trend with increasing volatility (Fig. 13b). A Yorkfit (Isoplot v.4.0) regression through all HSE from these metals shows that Pd is rejected as an outlier from this correlation. The overall depletion of HSE with increasing

volatility in carbonaceous chondrite metal is distinct from the patterns observed for ordinary chondrite metal (Okabayashi et al., 2019; Archer et al., 2019). For these non-carbonaceous chondrites, although with large errors due to intra-grain variability, relatively flat HSE patterns are observed (Okabayashi et al. 2019, Fig. 13). This suggests that either the chondrule precursors or the physicochemical conditions of chondrule formation were different between ordinary and carbonaceous chondrite chondrules.

In Fig. 13d–f, we show the HSE volatility patterns of core and rim metals from CV, CR and CM chondrites, respectively. Key observations taken from these figures can help to constrain the origin of the HSE patterns. First, while core metal compositions of CV, CR and CM chondrites are nearly identical, the rim metals vary between chondrite groups. In detail, the rim HSE concentrations of CR and CM chondrites are close to or lower than the core HSE concentrations, whereas the rim metal grains analyzed from the CV chondrite all have higher HSE concentrations. Nevertheless, all rim metals show similar HSE depletion trends with increasing volatility. If we consider the possibility of HSE precursor mixing according to Palme (2008), where the most refractory HSE are located in different precursors than Pd and Au according to their condensation temperatures, we use the regressions only through the most refractory HSE (i.e., Os, Ir, Ru, Pt, Rh). Within this consideration, Pd and Au often do not lie on these regression lines (Fig. 13d–f). Moreover, while the most refractory HSE all correlate with Ir according to their volatility (Fig. S3a), Pd and Au are not correlated with either refractory HSE or each other (Fig. S3b). For CV chondrites, in the core metals, Pd is enriched relative to the HSE regression line (red box, Fig. 13d), whereas Pd is relatively depleted in the rim metals. In all cases (e.g., CV chondrule rims and cores), Au falls on the regression lines. For CR and CM chondrites, both Pd and Au are enriched relative to the refractory HSE regression lines in the core and rim metals (red boxes, Fig. 13e, f).

We have looked at potential precursor materials of chondrules to find an explanation for these typical volatility trends of HSE in metal from carbonaceous chondrites (Fig. 13b). We consider here the pristine compositions of RMNs as precursors of chondritic metal. For this, we used the average RMN composition from a large dataset of carbonaceous chondrite RMNs (Daly et al., 2017) and have converted the atomic weight percentages of HSE to weight percentages normalized to CI chondrites, so we can compare the thus obtained HSE ratios to those of chondritic metals. The Os/Ir (1.3) and Os/Rh (1.8) ratios of RMNs are indistinguishable within error from those of chondrule core metals (Os/Ir = 1.1, Os/Rh = 1.9), although the absolute concentrations of refractory HSE within RMN are much higher relative to CI chondrites (Fig. 15). Pd and Au in RMNs were not analyzed by Daly et al. (2017), but RMN condensation models suggest that the concentrations of Pd and Au are depleted relative to CI in RMN at disk temperatures between 1900 and 1400 K (Campbell et al., 2003). As mentioned above, Pd and Au are suggested to condense together with FeNi alloys at lower disk temperatures (<1350 K) (Palme, 2008). At that point, since the more refractory HSE already condensed in RMN, these metal alloys will be depleted in Os, Ir, Ru, Pt and Rh relative to CI chondrites (Fig. 15). Such FeNi alloy precursor condensates are predicted but have not actually been identified and analyzed as such in meteorites. Nevertheless, we use the Pd/Au ratio of bulk Fremdlinge (>2.3, Au below detection limit) as a proxy in Fig. 15 (Campbell et al., 2003), which is similar to the Pd/Au ratio of the average chondrite core metal (Pd/Au = 3.2). The absolute concentrations of Pd and Au in Fremdlinge are higher than in chondrite metal by a factor 2–3, but it is very uncertain what the concentration would have been in pure FeNi precursor alloys. In addition, considering the solubility of Pd and Au in silicates (Borisov et al., 1994), we should expect Pd and Au to condense onto chondrule silicate precursors as well. These silicates should have similar HSE patterns as FeNi alloys (Fig. 15).

If these three precursors – RMNs, FeNi alloys and silicates – equilibrate with each other at chondrule formation temperatures (>1800 K), it is possible to form a chondrite metal HSE pattern as observed in our samples (Fig. 13b). During equilibration of RMN with FeNi and silicates, all HSE are expected to stay in the metal phase. The equilibrated metal liquid that forms will lower the absolute concentrations of the most refractory HSE, since these are being diluted by addition Fe, Ni, and other minor elements. Based on the concentrations of refractory HSE in RMNs ($\sim$1–2 $\times$ 10^5/CI), only a minute fraction ($\ll$1%) of RMNs is needed to raise the chondrite metal concentration of HSEs to 10$\times$ CI. However, since the abundance of refractory HSE added to this new metal from the FeNi and silicate precursors is insignificant, the RMN HSE pattern is preserved in the equilibrated metal. In contrast, the Pd and Au concentrations in RMNs are low (<CI, (Campbell et al., 2003)), and the equilibrated metal acquires these HSE from FeNi as well as silicate precursors. Then, depending on the temperature and redox conditions of chondrule formation, Pd and Au will be more or less concentrated in the final metal (Borisov and Palme, 1995). Since the core metal HSE compositions of CV, CM and CR chondrules are very similar, this implies that the relative proportions and nature of precursor materials must have been the same as well.

Finally, we note that W and Mo are often considered refractory HSE that have similarly high condensation temperatures. The high W and Mo concentrations in chondritic metal could therefore be attributed to condensation of RMNs and subsequent aggregation to chondrule precursors. However, W and Mo are also highly susceptible to oxidation processes (Klöck et al., 1986; Walter and Thibault, 1995), where the metal-silicate partition coefficient of these elements significantly increases in a reducing environment. Moreover, at relatively low pressures (i.e., chondrule forming conditions at 100 Pa), it has been shown that Mo is significantly more siderophile (at least by an order of magnitude relative to mantle-core boundary pressure conditions; Walter and Thibault, 1995). This might be similar for W (Shofner, 2011). Hence, W and Mo cannot be used to distinguish between condensation or metal-silicate equilibration origins of chondrite metals.

4.5. Conditions of chondrule formation in CV, CR and CM chondrites

In the previous sections, we have argued for metal-silicate equilibration of precursor materials during chondrule formation based on HSE compositions and subsolar Co/Ni ratios of chondrule core metals. Here, we discuss the conditions of chondrule formation for CR, CM and CV chondrule populations and the behavior of siderophile and lithophile elements assuming metal and silicate equilibrated.

Although Co/Ni ratios of metal grains are constant between the various chondrule populations, their absolute Ni and Co ratios are not (Fig. 6). CR chondrules have significantly higher and less variant Ni compositions than CM, CM-an and CV chondrules (Table 1). During metal-silicate equilibration, this is an expected outcome of chondrule formation under relatively higher temperatures and/or more oxidizing conditions (Capobianco and Amelin, 1994; Holzheid and Palme, 1996). The overall volatility patterns of CR chondrule core metals suggests that CR chondrules were formed in more oxidizing environments than CV chondrules (Fig. 11c). The typically elevated concentrations of W, Mo, V, Si, Cr, Mn, Cu, Zn and Sn in CV relative to CR chondrule metals indicate that the former equilibrated in more reduced conditions (Wade and Wood, 2005; Mann et al., 2009).

If the enrichments in moderately siderophile elements in CV relative to CR metals reflect reducing conditions in the CV chondrule formation region, then by extension, Paris metal volatility patterns are indicative of both CV- and CR-like chondrule forming conditions, since these patterns overlap both chondrule types (Fig. 11d). As a side note, it is unclear whether Paris chondrules are representative of CM chondrules in general. Even though Paris and Maribo share a similarly low degree of aqueous alteration, their metal abundances, H isotope signatures and organic matter inventory may reflect different origins (Hewins et al., 2014; Piani et al., 2018; van Kooten et al., 2018). The H isotope compositions of CM phyllosilicates suggest that Maribo, rather than Paris, reflects a relatively unaltered sample of stereotypical CM chondrites (Piani et al., 2018; van Kooten et al., 2018). Here, we show that the metal volatility patterns of Maribo are also distinct from Paris metal grains. Both silicate and metal volatility patterns from Maribo are relatively flat and close to a CI chondrite composition (van Kooten et al., 2019, this study), suggesting limited volatile loss during chondrule formation. In contrast, metal grains from Paris chondrules do reflect volatile loss, which in turn implies that Paris and Maribo chondrules formed during different chondrule formation events, separated by space and/or time. Finally, some core and rim metal grains from Paris have increased and correlated Cr and Si abundances (Fig. S4c). These have been interpreted as reflecting decreasing oxygen fugacity in the chondrule forming regions associated with these metal grains (Zanda et al., 1994). However, one of these grains (ch5), with abundant inclusions, uniquely lies on the solar Co/Ni correlation (Fig. 5a). This suggests that the chondrule metal, possibly originally formed by condensation, escaped significant re-equilibration during melting. Likewise, other Paris metal grains with correlated Cr and Si abundances (both elements having similar condensation temperatures), may reflect condensates rather than equilibrated metals, in agreement with Section 4.2.

The anomalous CM-chondrite Bells has metal volatility patterns that cannot be directly related to CR, CV or CM chondrite metals (Fig. 11a and b). The Bells chondrule core metal most closely resembles that of Paris chondrule rim metal (e.g. Ch4 and Ch13), but the sample size of the Bells chondrule population is too low to place firm constraints. The isolated metal grains from Bells show very distinct volatility patterns from the chondrule core metals. These grains are characterized by high Ni and Co contents, only seen in CH chondrite zoned metal grains (Ni = 5–14 wt.%) that have been linked to condensation processes in the solar nebula (Campbell and Humayun, 2004). CH metal grain compositions are mostly within range of Bells isolated grains, except for the most refractory HSE (e.g., Os, Ir and Ru), which are more concentrated in Bells by a factor <2. This could suggest some genetic link between metal-rich carbonaceous chondrite metal and Bells metal, which is in agreement with the previously suggested link between CM and another group of metal-rich carbonaceous chondrites, the CR chondrites (van Kooten et al., 2020). For example, the addition of RMNs to CH metal grains and subsequent equilibration between these metals and silicates could explain the volatility patterns of Bells isolated grains.

4.6. Isolated metal grains

We have discussed above the likely distinct origin of isolated grains relative to chondrule metal grains from the anomalous Bells chondrite. Isolated metal grains from the chondrite matrix, which are petrolographically detached from chondrules, have sparked interest with respect to the complementarity debate. In detail, the accretion of expelled chondrule metal to the matrix has been suggested to result in chondrule-matrix complementarity of siderophile elements (Budde et al., 2016b, a; Hezel et al., 2018). The volatility patterns of CR and CM (Paris) isolated metal grains are indistinguishable from corresponding chondrule core and rim metals (Figs. 7 and 8). Like CR chondrule rim metals, the isolated grains may have experienced lower metal-silicate equilibration temperatures than the core metal, based on their Ni and Co contents. Paris isolated metal grains often contain small silicate rims attached to the metal phase, implying that these metals were/are indeed originally part of a chondrule. Most isolated metal grains analyzed here are relatively large and of a similar order of size as the chondrules (>100 μm). Assuming our dataset is not subject to a sampling bias, this suggests that chondrule transport to the final chondrite accretion region, even if exposed to a size sorting effect in the protoplanetary disk, would have involved both chondrules and these expelled metal grains (van Kooten et al., 2019). Hence, we cannot justify a complementarity scenario, where expelled metal grains would have accreted directly to the matrix present in the chondrule forming reservoir as envisioned by Hezel et al. (2018). Interestingly, the smaller isolated metal grains

analyzed from Maribo (<20 μm) have relatively flat volatility patterns, closer in composition to CI chondrites (Fig. 8). It is unclear whether small metal grains in the chondrite matrix can be related to chondrule formation, or if they represent relatively unprocessed dust from the solar nebula.

5. CONCLUSIONS

We report on the major, minor and trace element compositions from CR, CV and CM carbonaceous chondrite metal grains. The relatively low degree of secondary alteration recorded by our selected samples (e.g. Paris, Maribo, NWA 801, Leoville and Bells) allows us to place the following constraints on the nature of metal precursors and the physicochemical conditions of chondrule formation:

- We observe a predominant and constant sub-solar Co/Ni ratio of CR, CM and CM-an metal grains and possibly for CV metal grains, which typically exhibit redistribution of Ni from secondary thermal metamorphism. In Ni versus Co space, the metal grains fall below modelled curves for equilibrium condensation of metals from a solar gas. From Ni versus Cr plots, we infer that Paris metal grains can be interpreted as having maintained a primary condensation signature, although for most grains, disequilibrium condensation needs to be invoked. CR and CM-an metals mostly fall outside of the predicted condensation fields and we interpret their Co/Ni and Cr/Ni signatures as having a planetary origin and were presumably extracted by impact jetting. Considering that almost all CM and CR metal grains have the same Co/Ni ratio, we cannot rule out a planetary origin for CM metal grains.
- HSE volatility patterns of CV, CR and CM chondrite metals have identical CI-normalized decreasing HSE abundances with increasing volatility. We suggest that these patterns are the result of mixing and subsequent equilibration of RMN, FeNi alloy and silicate chondrule precursors. Since the core metal HSE compositions of CV, CM and CR chondrules are very similar, this implies that the relative proportions and nature of precursor materials must have been the same as well. Relative to previous analyses of ordinary chondrite metals with flat HSE patterns, the negative slope of HSE abundances with increasing volatility can be attributed to an increased abundance of refractory metal precursors in the carbonaceous chondrule forming region(s).
- We suggest that the chondrule rim metals are derived from the equilibrated cores, and, subsequently accreted additional RMN-like grains that did not fully equilibrate with the original metal rims.
- The overall volatility patterns of CV, CM and CR chondrites, suggest that the latter form under more oxidizing conditions than CV and CM chondrites.
- Trace element analyses of Bells metal grains show potential relationships with CM chondrite and CH chondrite metal for the chondrule cores and isolated grains, respectively. This agrees with previous Cr and Mg isotope analyses, identifying Bells as transition material between CM and metal-rich carbonaceous chondrites.
- Large isolated metal grains from CR and CM (Paris) chondrites are identical to chondrule metals, suggesting they were expelled during chondrule formation. Small metal grains from CM chondrite Maribo, which are located in the chondrite matrix, show distinct volatility patterns from CR and Paris IGs, hinting at a distinct origin for small metal grains and large chondrule-derived metal grains. This distinction should be further explored.

Declaration of Competing Interest

The authors declare that they have no known competing financial interests or personal relationships that could have appeared to influence the work reported in this paper.

ACKNOWLEDGEMENTS

We thank prof. Herbert Palme and two anonymous reviewers for offering their valuable expertise, which has significantly improved this manuscript. This project has received funding from the European Union's Horizon 2020 research and innovation programme under the Marie Skłodowska-Curie Grant Agreement No 786081 to E.v.K. F.M. acknowledges funding from the European Research Council under the H2020 framework program/ERC grant agreement no. 637503 (Pristine) and financial support of the UnivEarthS Labex program at Sorbonne Paris Cité (ANR-10-LABX-0023 and ANR-11-IDEX-0005-02). Parts of this work were supported by IPGP multidisciplinary PARI program, and by Region Île-de-France SESAME Grant no. 12015908. We thank the Natural History Museum of Denmark for the loan of Leoville, NWA 801, Maribo and Bells meteorites and the Natural History Museum of Paris for the loan of section 4029sp3 (2010-3, B1.5) from the Paris meteorite.

APPENDIX A AND B. SUPPLEMENTARY MATERIAL

Supplementary data to this article can be found online at https://doi.org/10.1016/j.gca.2022.01.008.

REFERENCES

Abreu N. M. and Brearley A. J. (2005) Carbonates in Vigarano: Terrestrial, preterrestrial, or both? *Meteorit. Planet. Sci.* **40**, 609.

Archer G. J., Walker R. J., Tino J., Blackburn T., Kruijer T. S. and Hellmann J. L. (2019) Siderophile element constraints on the thermal history of the H chondrite parent body. *Geochim. Cosmochim. Acta* **245**, 556–576.

Asphaug E., Jutzi M. and Movshovitz N. (2011) Chondrule formation during planetesimal accretion. *Earth Planet. Sci. Lett.* **308**, 369–379.

Bonal L., Quirico E., Bourot-Denise M. and Montagnac G. (2006) Determination of the petrologic type of CV3 chondrites by Raman spectroscopy of included organic matter. *Geochim. Cosmochim. Acta* **70**, 1849–1863.

Bonal L., Quirico E., Flandinet L. and Montagnac G. (2016) Thermal history of type 3 chondrites from the Antarctic meteorite collection determined by Raman spectroscopy of their polyaromatic carbonaceous matter. *Geochim. Cosmochim. Acta* **189**, 312–337.

Boom R., De Boer F. R., Niessen A. K. and Miedema A. R. (1983) Enthalpies of formation of liquid and solid binary alloys based on 3d metals: III. Alloys of iron. *Phys. BC* **115**, 285–309.

Borisov A. and Palme H. (1995) Metal/Silicate/Sulfide Partitioning of Highly Siderophile Elements (HSE) as Derived from Recent Solubility Data. In *Abstracts of the Lunar and Planetary Science Conference*, 26, p. 147. Abstracts of the Lunar and Planetary Science Conference.

Borisov A., Palme H. and Spettel B. (1994) Solubility of palladium in silicate melts: Implications for core formation in the Earth. *Geochim. Cosmochim. Acta* **58**, 705–716.

Bourot-Denism M., Zanda B., Marrocchi Y., Greenwood R. C., Pont S., Hewins R. H., Franchi I. A. and Cornen G. (2010) Paris: The slightly altered, slightly metamorphosed CM that bridges the gap between CMs and Cos. *41st Lunar and Planetary Science Conference. Houston, Texas*.

Brearley A. J. (1995) Aqueous alteration and brecciation in Bells, an unusual, saponite-bearing, CM chondrite. *Geochim. Cosmochim. Acta* **59**, 2291–2317.

Briani G., Quirico E., Gounelle M., Paulhiac-Pison M., Montagnac G., Beck P., Orthous-Daunay F.-R., Bonal L., Jacquet E., Kearsley A. and Russell S. S. (2013) Short duration thermal metamorphism in CR chondrites. *Geochim. Cosmochim. Acta* **122**, 267–279.

Budde G., Burkhardt C., Brennecka G. A., Fischer-Gödde M., Kruijer T. S. and Kleine T. (2016a) Molybdenum isotopic evidence for the origin of chondrules and a distinct genetic heritage of carbonaceous and non-carbonaceous meteorites. *Earth Planet. Sci. Lett.* **454**, 293–303.

Budde G., Kleine T., Kruijer T. S., Burkhardt C. and Metzler K. (2016b) Tungsten isotopic constraints on the age and origin of chondrules. *Proc. Natl. Acad. Sci.* **113**, 2886–2891.

Campbell A. J. and Humayun M. (2005) Compositions of group IVB iron meteorites and their parent melt. *Geochim. Cosmochim. Acta* **69**, 4733–4744.

Campbell A. J. and Humayun M. (2003) Formation of metal in Grosvenor Mountains 95551 and comparison to ordinary chondrites. *Geochim. Cosmochim. Acta* **67**, 2481–2495.

Campbell A. J. and Humayun M. (2004) Formation of metal in the CH chondrites ALH 85085 and PCA 91467. *Geochim. Cosmochim. Acta* **68**, 3409–3422.

Campbell A. J., Humayun M., Meibom A., Krot A. N. and Keil K. (2001) Origin of zoned metal grains in the QUE94411 chondrite. *Geochim. Cosmochim. Acta* **65**, 163–180.

Campbell A. J., Simon S. B., Humayun M. and Grossman L. (2003) Chemical evolution of metal in refractory inclusions in CV3 chondrites. *Geochim. Cosmochim. Acta* **67**, 3119–3134.

Capobianco C. J. and Amelin A. A. (1994) Metal-silicate partitioning of nickel and cobalt: The influence of temperature and oxygen fugacity. *Geochim. Cosmochim. Acta* **58**, 125–140.

Charles C. R. J., Robin P.-Y.-F., Davis D. W. and McCausland P. J. A. (2018) Shapes of chondrules determined from the petrofabric of the CR2 chondrite NWA 801. *Meteorit. Planet. Sci.* **53**, 935–951.

Connolly H. C., Huss G. R. and Wasserburg G. J. (2001) On the formation of Fe-Ni metal in Renazzo-like carbonaceous chondrites. *Geochim. Cosmochim. Acta* **65**, 4567–4588.

Daly L., Bland P. A., Dyl K. A., Forman L. V., Evans K. A., Trimby P. W., Moody S., Yang L., Liu H., Ringer S. P., Ryan C. G. and Saunders M. (2017) In situ analysis of Refractory Metal Nuggets in carbonaceous chondrites. *Geochim. Cosmochim. Acta* **216**, 61–81.

Gilmour C. M. and Herd C. D. K. (2020) In situ analysis of platinum group elements in equilibrated ordinary chondrite kamacite and taenite. *Meteorit. Planet. Sci.* **55**, 679–702.

Grossman J. N. and Wasson J. T. (1985) The origin and history of the metal and sulfide components of chondrules. *Geochim. Cosmochim. Acta* **49**, 925–939.

Grossman L. and Olsen E. (1974) Origin of the high-temperature fraction of C2 chondrites. *Geochim. Cosmochim. Acta* **38**, 173–174.

Grossman L., Olsen E. and Lattimer J. M. (1979) Silicon in Carbonaceous Chondrite Metal: Relic of High-Temperature Condensation. *Science* **206**, 449–451.

Haack H., Grau T., Bischoff A., Horstmann M., Wasson J., Sørensen A., Laubenstein M., Ott U., Palme H., Gellissen M., Greenwood R. C., Pearson V. K., Franchi I. A., Gabelica Z. and Schmitt-Kopplin P. (2012) Maribo—A new CM fall from Denmark. *Meteorit. Planet. Sci.* **47**, 30–50.

Harju E. R., Rubin A. E., Ahn I., Choi B.-G., Ziegler K. and Wasson J. T. (2014) Progressive aqueous alteration of CR carbonaceous chondrites. *Geochim. Cosmochim. Acta* **139**, 267–292.

Hewins R. H., Bourot-Denise M., Zanda B., Leroux H., Barrat J.-A., Humayun M., Göpel C., Greenwood R. C., Franchi I. A., Pont S., Lorand J.-P., Cournède C., Gattacceca J., Rochette P., Kuga M., Marrocchi Y. and Marty B. (2014) The Paris meteorite, the least altered CM chondrite so far. *Geochim. Cosmochim. Acta* **124**, 190–222.

Hezel D. C., Harak M. and Libourel G. (2018) What we know about elemental bulk chondrule and matrix compositions: Presenting the ChondriteDB Database. *Geochemistry* **78**, 1–14.

Holzheid A. and Palme H. (1996) The influence of FeO on the solubilities of cobalt and nickel in silicate melts. *Geochim. Cosmochim. Acta* **60**, 1181–1193.

Hultgren R., Desai P. D., Hawkins D. T., Gleiser M. and Kelley K. (1973) *Selected Values of the Thermodynamic Properties of Binary Alloys*. American Society for Metals, the University of Virginia, Metals Park, Ohio.

Humayun M. (2012) Chondrule cooling rates inferred from diffusive profiles in metal lumps from the Acfer 097 CR2 chondrite. *Meteorit. Planet. Sci.* **47**, 1191–1208.

Humayun M. and Campbell A. J. (2002) The duration of ordinary chondrite metamorphism inferred from tungsten microdistribution in metal. *Earth Planet. Sci. Lett.* **198**, 225–243.

Hyde B. C., Day J. M. D., Tait K. T., Ash R. D., Holdsworth D. W. and Moser D. E. (2014) Characterization of weathering and heterogeneous mineral phase distribution in brachinite Northwest Africa 4872. *Meteorit. Planet. Sci.* **49**, 1141–1156.

Jacquet E. (2021) Collisions and compositional variability in chondrule-forming events. *Geochim. Cosmochim. Acta* **296**, 18–37.

Jacquet E., Paulhiac-Pison M., Alard O., Kearsley A. T. and Gounelle M. (2013) Trace element geochemistry of CR chondrite metal. *Meteorit. Planet. Sci.* **48**, 1981–1999.

Johnson B. C., Minton D. A., Melosh H. J. and Zuber M. T. (2015) Impact jetting as the origin of chondrules. *Nature* **517**, 339–341.

Kadlag Yogit, Tatzel Michae, Frick Danie and Becker Harr, et al. (2019) The origin of unequilibrated EH chondrites - constraints from in-situ analysis of Si isotopes, major and trace elements in silicates and metal. *Geochim. Cosmochim. Acta* **267**, 300–321.

Kallemeyn G. W. (1995) Bells and Essebi: To Be or Not To Be (CM). *Meteoritics* **30**.

Kegler P. h., Holzheid A., Frost D. J., Rubie D. C., Dohmen R. and Palme H. (2008) New Ni and Co metal-silicate partitioning

data and their relevance for an early terrestrial magma ocean. *Earth Planet. Sci. Lett.* **268**, 28–40.
Kimura M. (1988) Origin of opaque minerals in an unequilibrated enstatite chondrite Yamato-691. *Antarct. Meteor. Res.* **1**, 51.
Kimura M., Grossman J. N. and Weisberg M. K. (2011) Fe-Ni metal and sulfide minerals in CM chondrites: An indicator for thermal history. *Meteorit. Planet. Sci.* **46**, 431–442.
Klöck W., Palme H. and Tobschall H. (1986) Trace elements in natural metallic iron from Disko Island, Greenland. *Contrib. Mineral. Petrol.* **93**, 273–282.
Kong P. and Ebihara M. (1997) The origin and nebular history of the metal phase of ordinary chondrites. *Geochim. Cosmochim. Acta* **61**, 2317–2329.
van Kooten E. M. M. E., Cavalcante L. L., Nagashima K., Kasama T., Balogh Z. I., Peeters Z., Hsiao S.-S.-Y., Shang H., Lee D.-C., Lee T., Krot A. N. and Bizzarro M. (2018) Isotope record of mineralogical changes in a spectrum of aqueously altered CM chondrites. *Geochim. Cosmochim. Acta* **237**, 79–102.
van Kooten E., Cavalcante L., Wielandt D. and Bizzarro M. (2020) The role of Bells in the continuous accretion between the CM and CR chondrite reservoirs. *Meteorit. Planet. Sci.* **55**, 1–16.
van Kooten E. and Moynier F. (2019) Zinc isotope analyses of singularly small samples (<5 ng Zn): investigating chondrule-matrix complementarity in Leoville. *Geochim. Cosmochim. Acta* **261**, 248–268.
van Kooten E., Moynier F. and Agranier A. (2019) A unifying model for the accretion of chondrules and matrix. *Proc. Natl. Acad. Sci.* **116**, 18860–18866.
van Kooten E., Wielandt D., Schiller M., Nagashima K., Thomen A., Larsen K., Olsen M., Nordlund A., Krot A. and Bizzarro M. (2016) Isotopic evidence for primordial molecular cloud material in metal-rich carbonaceous chondrites. *Proc. Natl. Acad. Sci.* **113**, 2011–2016.
Krot A. N., Meibom A., Weisberg M. K. and Keil K. (2002) The CR chondrite clan: Implications for early solar system processes. *Meteorit. Planet. Sci.* **37**, 1451–1490.
Kruijer T., Burkhardt C, Budde G. and Kleine T (2017) Age of Jupiter inferred from the distinct genetics and formation times of meteorites. *Proc. Natl. Acad. Sci.* **114**, 6712–6716.
Lee M. S., Rubin A. E. and Wasson J. T. (1992) Origin of metallic Fe-Ni in Renazzo and related chondrites. *Geochim. Cosmochim. Acta* **56**, 2521–2533.
Lehner S. W., Buseck P. R. and McDonough W. F. (2010) Origin of kamacite, schreibersite, and perryite in metal-sulfide nodules of the enstatite chondrite Sahara 97072 (EH3). *Meteorit. Planet. Sci.* **45**, 289–303.
Li J. and Agee C. B. (1996) Geochemistry of mantle-core differentiation at high pressure. *Nature* **381**, 686–689.
Lichtenberg T., Golabek G. J., Dullemond C. P., Schönbächler M., Gerya T. V. and Meyer M. R. (2018) Impact splash chondrule formation during planetesimal recycling. *Icarus* **302**, 27–43.
Lin Y. and Goresy A. E. (2002) A comparative study of opaque phases in Qingzhen (EH3) and MacAlpine Hills 88136 (EL3): Representatives of EH and EL parent bodies. *Meteorit. Planet. Sci.* **37**, 577–599.
Lodders K. (2003) Solar System Abundances and Condensation Temperatures of the Elements. *Astrophys. J.* **591**, 1220.
Mann U., Frost D. J. and Rubie D. C. (2009) Evidence for high-pressure core-mantle differentiation from the metal–silicate partitioning of lithophile and weakly-siderophile elements. *Geochim. Cosmochim. Acta* **73**, 7360–7386.
Marrocchi Y. and Libourel G. (2013) Sulfur and sulfides in chondrules. *Geochim. Cosmochim. Acta* **119**, 117–136.
Marrocchi Y., Villeneuve J., Batanova V., Piani L. and Jacquet E. (2018) Oxygen isotopic diversity of chondrule precursors and the nebular origin of chondrules. *Earth Planet. Sci. Lett.* **496**, 132–141.
Martin P. M., Mills A. A. and Walker E. (1975) Preferential orientation in four C3 chondritic meteorites. *Nature* **257**, 37–38.
Meibom A., Petaev M. I., Krot A. N., Wood J. A. and Keil K. (1999) Primitive FeNi metal grains in CH carbonaceous chondrites formed by condensation from a gas of solar composition. *J. Geophys. Res. Planets* **104**, 22053–22059.
Mittlefehldt D. W. (2002) Geochemistry of the ungrouped carbonaceous chondrite Tagish Lake, the anomalous CM chondrite Bells, and comparison with CI and CM chondrites. *Meteorit. Planet. Sci.* **37**, 703–712.
Nagashima K., Krot A. N. and Huss G. R. (2015) Oxygen-isotope compositions of chondrule phenocrysts and matrix grains in Kakangari K-grouplet chondrite: Implication to a chondrule-matrix genetic relationship. *Geochim. Cosmochim. Acta* **151**, 49–67.
Nakanishi N., Yokoyama T., Okabayashi S., Iwamori H. and Hirata T. (2021) Geochemical constraints on the formation of chondrules: Implication from Os and Fe isotopes and HSE abundances in metals from CR chondrites. *Geochim. Cosmochim. Acta*.
Okabayashi S., Yokoyama T., Nakanishi N. and Iwamori H. (2019) Fractionation of highly siderophile elements in metal grains from unequilibrated ordinary chondrites: Implications for the origin of chondritic metals. *Geochim. Cosmochim. Acta* **244**, 197–215.
Palme H. (2008) Platinum-Group Elements in Cosmochemistry. *Elements* **4**, 233–238.
Paton C., Hellstrom J., Paul B., Woodhead J. and Hergt J. (2011) Iolite: Freeware for the visualisation and processing of mass spectrometric data. *J. Anal. At. Spectrom.* **26**, 2508–2518.
Piani L., Yurimoto H. and Remusat L. (2018) A dual origin for water in carbonaceous asteroids revealed by CM chondrites. *Nat. Astron.* **2**, 317–323.
Pignatelli I., Marrocchi Y., Mugnaioli E., Bourdelle F. and Gounelle M. (2017) Mineralogical, crystallographic and redox features of the earliest stages of fluid alteration in CM chondrites. *Geochim. Cosmochim. Acta* **209**, 106–122.
Pringle E. A., Moynier F., Beck P., Paniello R. and Hezel D. C. (2017) The origin of volatile element depletion in early solar system material: Clues from Zn isotopes in chondrules. *Earth Planet. Sci. Lett.* **468**, 62–71.
Righter K. (2003) Metal-Silicate Partitioning of Siderophile Elements and Core Formation in the Early Earth. *Annu. Rev. Earth Planet. Sci.* **31**, 135–174.
Rubin A. E., Trigo-Rodríguez J. M., Huber H. and Wasson J. T. (2007) Progressive aqueous alteration of CM carbonaceous chondrites. *Geochim. Cosmochim. Acta* **71**, 2361–2382.
Sanders I. S. and Scott E. R. D. (2018) Making Chondrules by Splashing Molten Planetesimals: The Dirty Impact Plume Model. In *Chondrules: Records of Protoplanetary Disk Processes* (eds. A. N. Krot, H. C. Connolly and S. S. Russell). Cambridge Planetary Science. Cambridge University Press, Cambridge, pp. 361–374.
Schrader D. L., Franchi I. A., Connolly H. C., Greenwood R. C., Lauretta D. S. and Gibson J. M. (2011) The formation and alteration of the Renazzo-like carbonaceous chondrites I: Implications of bulk-oxygen isotopic composition. *Geochim. Cosmochim. Acta* **75**, 308–325.
Scott E. R. D. and Krot A. N. (2014) 1.2 – Chondrites and Their Components. In *Treatise on Geochemistry (Second Edition)* (eds. H. D. Holland and K. K. Turekian). Elsevier, Oxford, pp. 65–137.

Shofner G. (2011) *High Pressure Redox Geochemistry of Tungsten in Metal-silicate Systems: Implications for Core Formation in the Earth*. University of Maryland.

Visser R., John T., Patzek M., Bischoff A. and Whitehouse M. J. (2019) Sulfur isotope study of sulfides in CI, CM, C2ung chondrites and volatile-rich clasts – evidence for different generations and reservoirs of sulfide formation. *Geochim. Cosmochim. Acta*.

Wade J. and Wood B. J. (2005) Core formation and the oxidation state of the Earth. *Earth Planet. Sci. Lett.* **236**, 78–95.

Walter M. J. and Thibault Y. (1995) Partitioning of Tungsten and Molybdenum Between Metallic Liquid and Silicate Melt. *Science* **270**, 1186–1189.

Warren P. (2011) Stable-isotopic anomalies and the accretionary assemblage of the Earth and Mars: A subordinate role for carbonaceous chondrites. *Earth Planet. Sci. Lett.* **311**, 93–100.

Wasson J. T. and Rubin A. E. (2010) Metal in CR chondrites. *Geochim. Cosmochim. Acta* **74**, 2212–2230.

Wood B. J., Smythe D. J. and Harrison T. (2019) The condensation temperatures of the elements: A reappraisal. *Am. Mineral.* **104**, 844–856.

Zanda B., Bourot-Denise M., Perron C. and Hewins R. H. (1994) Origin and Metamorphic Redistribution of Silicon, Chromium, and Phosphorus in the Metal of Chondrites. *Science* **265**, 1846–1849.

Associate editor: Yves Marrocchi